Constraining neotectonic deformation of the Colombian sub-Andes

By

Erica M Dalman

Submitted to the graduate degree program in Geology and the Graduate Faculty of the University of Kansas in partial fulfillment of the requirements for the degree of Master of Science.

_____

Chairperson Michael Taylor

_____

Jennifer Roberts

_____

Doug Walker

Date Defended: March 2, 2015

The Thesis Committee for Erica M Dalman

certifies that this is the approved version of the following thesis:

Constraining neotectonic deformation of the Colombian sub-Andes

_____

Chairperson Michael Taylor

_____

Jennifer Roberts

_____

Doug Walker

Date approved: March 2, 2015

Abstract

The eastern foothills of the Eastern Cordillera of the Colombian Andes are actively shortening; however, deformation rates of Quaternary structures remain sparse. Here we present millennia-scale deformation rates of the Guaicaramo thrust in the Eastern Cordillera using Terrestrial in situ Cosmogenic Nuclide dating techniques. Furthermore, we analyze river profiles along strike using digital elevation models to quantify the fluvial response to uplift. This research provides insight into thrust wedge mechanics and dynamics, seismic hazard mitigation, and hydrocarbon production potential of the region. The Quaternary shortening rate of the Guaicaramo thrust is 1.72 ± 0.30 mm/yr, which represents ~3% of the total horizontal shortening across the Colombian Andes. Furthermore, the normalized channel steepness (k_{sn}) values reflect that the Eastern Cordillera foothills are experiencing rapid uplift. Analysis of k_{sn} is a novel approach in the region. This work provides quantitative metrics of the surface response to uplift along the eastern foothills of the Eastern Cordillera.

Acknowledgements

"Plans fail for lack of counsel, but with many advisers they succeed." Proverbs 15:22.

This degree would not have been possible without the support of many people. I would like to thank my advisor, Mike Taylor, for taking me on as a student, for helping and guiding me throughout this process, and for exposing me to the tectonics of the Canadian Rockies, Iceland, and Colombia. I also thank my committee members, Jennifer Roberts and Doug Walker, for their feedback and support. I am very grateful to the Department of Geology, Kansas Geological Foundation, AAPG Grants-in-aid, and Ecopetrol-ICP for funding this project.

I am indebted to Gabriel Veloza for the countless hours he helped me with this project and his constant willingness to answer all of my questions. Thank you also to John Gosse, were it not for him I'd still be stuck in the basement of Lindley running models. Tom Clifton and Greg Chmiel guided the laboratory portion of this work. I must also acknowledge the Colombian land owners for letting us dig holes on their properties. Thank you also to Camilo and Martín for helping dig what seemed to be grave-sized holes.

I am grateful also for the help of my peers. There are too many to list here, but I'm grateful for the friendships I made while in the trenches of graduate school.

Thank you, Mom and Dad, for your constant encouragement, even when you had no idea what I was doing.

Finally, I would not be a geologist were it not for my high school Earth Science and Geology teacher, Chris Bolhuis. His passion for geology and teaching is truly contagious and will forever inspire me.

Table of Contents

Quantifying active deformation along the Eastern Cordillera of the Colombian Andes using terrestrial cosmogenic nuclide chronology and fluvial geomorphology

Erica Dalman[1#]

Michael Taylor[1]

Gabriel Veloza[1]

Andrés Mora[2]

[1]Department of Geology

University of Kansas

Lawrence, KS 66045

[2]ICP-Ecopetrol

Bucaramanga, Colombia

#Email address: edalman@ku.edu

To be submitted to Tectonics

Abstract

The eastern foothills of the Eastern Cordillera are actively shortening; however, deformation rates of Quaternary structures in the eastern foothills of the Colombian Andes remain sparse. Here we present millennia-scale deformation rates in the Eastern

Cordillera using Terrestrial in situ Cosmogenic Nuclide dating techniques, as well as analysis of digital elevation models and seismic reflection data. Two uplifted and deformed terraces in the hanging wall of the Guaicaramo thrust were dated using the ^{10}Be depth profiling method. The surface abandonment age for the two sites are 122^{+73}_{-4} *ka and* 117^{+83}_{-6} *111 ka. Total incision for each site varied significantly. The magnitude of incision at site 1 is 67 ± 6.6 m, while incision magnitude at site 2 is 131 ± 6.6 m. From these magnitudes, incision rates for each site are found to be 0.66 ± 0.1 mm/yr and 1.12 ± 0.22 mm/yr respectively. The difference in incision rates, despite the sites being of the same statistical surface exposure age is reconciled with a listric fault geometry with a flat on flat geometry in the hinterland where low incision values are observed. Larger incision magnitudes and rates are observed toward the foreland where the fault cuts up section over a hanging wall flat on footwall ramp geometry. Incision is only observed in the hanging wall of the front range thrusts, thus the rivers are incising as a direct response to tectonic uplift. Therefore, we used incision rates to calculate uplift and shortening rates. Quaternary shortening rates are 1.72 ± 0.30 mm/y. Thus, the Guaicaramo thrust is accommodating ~3% of the total horizontal shortening across the Colombian Andes.*

1. Introduction

Long term (10 to <10^6 years) slip rates of active faults are critical for understanding neotectonic deformation. Global Positioning Systems (GPS) provides short term rates of movement in active mountain belts, while tectonic reconstruction and thermochronology provide rates of fault slip over millions of years. However, only recently has it been possible to understand millennial-scale deformation rates along active faults (Tapponnier

et al., 2001). The advancement of in situ terrestrial cosmogenic nuclide (TCN) techniques has allowed researchers to begin filling in this gap by quantifying the geomorphic response to Quaternary uplift. One such geomorphic response is the deformation of fluvial terraces due to changes in local base levels as streams respond to orogenesis.

Studying deformation of geomorphic features, such as river terraces, is an important tool in understanding Quaternary fault kinematics and shortening in active fold and thrust belts (Amos et al., 2007; Lavé and Avouac, 2000; Lavé and Avouac, 2001; Simoes et al., 2007). Using in situ TCN geochronology, topography, and seismic reflection data, we present millennial scale deformation rates along the Guaicaramo thrust in the eastern foothills of the Eastern Cordillera (EC) of the Colombian Andes. Furthermore, we describe the geomorphic response of the upper reaches of fluvial systems to tectonic uplift by quantifying normalized stream channel steepness values (k_{sn}) across the EC. Our results provide insight into landscape response to uplift in the EC.

Understanding the structural and tectonic development of the Colombian Andes is important for three major reasons. (1) Constraining the geometry and kinematics of active faults in the EC is critical to our understanding of thrust wedge mechanics and dynamics. Studying continental deformation inboard of subduction boundaries is important in understanding how subduction controls the distribution of active faults in the upper plate (DeCelles et al., 2009). (2) Quantifying fault slip rates and identifying which faults are accommodating the highest shortening rates is critical for mitigation of seismic hazards. Earthquakes occurring in continental interiors are typically more devastating due to a paucity of identified fault locations and movements in such regions (England and Jackson, 2011). Additionally, the petroleum industry was responsible for 34% of Colombia's foreign

direct investment in 2012 (EIA, 2014), exemplifying the importance this sector has on the Colombian economy and the increasing interest from foreign companies. In the EC however, infrastructure in the region has been damaged due to shearing along active east-directed thrust faults. Quantifying the magnitude and rate of fault activity will aid in mitigating damages to existing and future petroleum infrastructure. (3) The Colombian sub-Andes is home to one of the largest on-shore conventional oil fields in Colombia, the Cusiana oil field (Cazier et al., 1995). Understanding the neotectonic setting, stress fields, fault geometry and kinematics, has proven critical to successfully developing the Cusiana field (Colmenares and Zoback, 2003; Last et al., 1995). Furthermore, the foothills of the EC have been called a “world-class prospective play” by Villamil (2003). Though the potential for oil exploration is high, the foothills remain largely unexplored. Knowing how active faults control the distribution of petroleum reserves (i.e., basin development) in continental settings is especially relevant for petroleum exploration (e.g., Taylor et al., 2012).

2. Background

2.1 Tectonic setting

The Colombian Andes are comprised of the Western, Central, and Eastern Cordilleras. The northern Andes are being deformed by eastward subduction of the Nazca plate from the west, the southeast subducting Caribbean plate to the north, and northeast motion of the South American plate from the east (Figure 1) (Gutscher et al., 1999; Taboada et al., 2000). However, it is still unclear how faulting at these plate boundaries

is actively partitioned into the South American plate (Mora et al., 2010; Parra et al., 2009). Geodetic shortening rates along the Venezuelan and Colombian Andes foothills indicate that the frontal thrusts are active (Pérez et al., 2011; Trenkamp et al., 2002). Furthermore, shallow seismicity in the region further indicates active faulting (Dimate et al., 2003; Veloza et al., 2012). Notable seismic events include the Tauramena 1995 Mw: 6.5 (Dimate et al., 2003) and more recent 2014 Mw: 5.4 Tame earthquakes (USGS, 2014).

The EC is a bivergent fold and thrust belt formed through reactivation of normal faults involving basement and metamorphic rocks, as well as Upper Paleozoic-Cenozoic sedimentary and volcanic rocks (Cortés et al., 2006; Mora et al., 2006; Toro et al., 2004). Cenozoic shortening rates since ~25Ma calculated for the EC vary between 1.2-2.1 mm/yr (Parra et al., 2009). The Guayaquil-Algeciras fault system bounds the EC to the south. This fault system extends to the northeast into the Llanos Basin and separates the Garzón Massif to the south (Mora et al., 2010; Veloza et al., 2012). The northern boundary of the EC is marked by the Santa Marta-Bucaramanga fault system (Veloza et al., 2012). The Llanos foothills along the eastern flank of the EC exposes folded Neogene rocks below uplifted fluvial deposits (Mora et al., 2010). West of the Guaicaramo thrust is the Servitá fault, which juxtaposes Upper Paleozoic and Pre-Devonian units over Paleogene and Neogene rocks in the hanging wall of the east directed Guaricaramo thrust fault (Mora et al., 2010).

2.2 Guaicaramo thrust

The frontal thrusts of the EC mark the tectonic boundary between the North Andean microplate and the South American Plate (Figure 2) (Aggarwal, 1983;

Freymueller et al., 1993). The eastern foothills are dominated by a NE-SW structural trend, with mainly E-SE directed thrust faults and folds. Borehole breakouts and earthquake focal mechanisms indicate the orientation of the maximum horizontal stress (S_{Hmax}) which is WNW-ESE, perpendicular to the structural grain. South of the Guaicaramo thrust, fold and fault orientations become more northerly. This is consistent with a change in the orientation of the S_{Hmax} from WNW-ESE to E-W (Colmenares and Zoback, 2003; Mora et al., 2010).

The Guaicaramo thrust is an east directed thin skinned thrust sheet dipping approximately 30° west. In the south, the Guaicaramo thrust detaches at depths of ~4km, but increases northward to a depth of ~13km as shortening increases and it steepens to a basement involved thrust, where it inverts a pre-existing extensional rift structure (Mora et al., 2006). Because of the differences in depth to detachment, and therefore the rocks it cuts (the timing of fault initiation), it has been proposed that the Guaicaramo thrust is a product of 2 fault segments merging (Mora et al., 2010). In the southern segment, a backthrust that extends to the surface is observed. The backthrust and Guaicaramo thrust are likely migrating southward (Mora et al., 2010). Geodetic shortening rates in the region (Villavicencio) indicate movement to the south at rates of 2.53 ± 1.29 mm/yr (1σ) (Trenkamp et al., 2002).

Deformation is observed in the hanging wall of the Guaicaramo thrust. Figure 2 highlights several neotectonic features. The Guavio anticline and Nazareth syncline are prominent features in the southern portion of the hanging wall and trend NE. East of the Nazareth syncline are smaller anticline-syncline pairs. The focus of this investigation is the uplifted and deformed fluvial terraces observed in the hanging wall of the Guaicaramo

thrust. However, east tilted Quaternary pediments in the footwall are a result of fault-propagation folds. Though no emergent thrusts are present east of the Guaicaramo thrust, the Cabuyarito anticline marks the easternmost active structure in the study area (Mora et al., 2010; Rowan and Linares, 2000) (Figure 2).

2.3 Climate

Climatic conditions have been shown to effect the landscape and evolution of orogens (Molnar et al., 1994; Molnar and England, 1990). Quaternary climate in the EC is characterized as a savannah, with expansive grass cover, but limited arboreal cover. Mean annual temperature in the foothills ranges from 18 to 24°C (IDEAM, 2012). Precipitation in the region has been shown to exert a strong control on landscape evolution, particularly in the Andes (Montgomery et al., 2001; Strecker et al., 2007). The difference in precipitation between the leeward and windward side in the EC is very pronounced. In the western leeward flank and Bogotá Basin, precipitation rates range from 1000 – 2000 mm/yr, while the eastern flank receives ~5000 mm/yr. Thus, the eastern foothills and Llanos Basin therefore receive some of the highest rainfall on Earth. Though Molnar and Cane (2002) hypothesize that northwest South America would have been drier in the Mid-Pliocene, others suggest that the humid climate and high precipitation rates have characterized the region since at least the Mid-Miocene (Hoorn, 1994; Mora et al., 2008; van der Hammen and Hooghiemstra, 2000). Paleoclimate data therefore suggest the EC was dominated by a tropical lowland climate (Hooghiemstra et al., 2006; Mora et al., 2008). The present orographic barrier is likely to have reached a critical

elevation between ca. 6 and ca. 3 Ma. The enhanced precipitation on the eastern flank therefore suggests high erosion rates (Mora et al., 2008).

Currently, only the northern portion of the EC in the Sierra Nevada del Cocuy is glaciated. However, the central and southern portions and specifically the Bogotá Basin have experienced Quaternary glaciation (Helmens, 1988; Helmens and Van der Hammen, 1994; Hooghiemstra, 1989). Based on field mapping and ^{14}C dating, Helmens (1988) identified at least 4 glacial periods in the late Pleistocene. Furthermore, pollen evidence indicates the region surrounding Bogotá has experienced periods of glaciations since 2.4 Ma (Helmens and Van der Hammen, 1994; Hooghiemstra, 1989).

The influence of climate in the long term mountain building history in the northern Andes has only recently been evaluated (Mora et al., 2008). East flowing streams on the eastern flank incise across the primary structural features, while those on the western flank do so only in a few locations and primarily flow parallel (north-south) to the orogen (Mora et al., 2008). While the influence of climate in enhancing orogenic thrusting is beyond the scope of this project, it is important nonetheless to consider the first-order impact of climate on erosion, depositional history of fluvial terraces, and development of the stream network.

3. Methods

3.1 Neotectonic mapping and field methods

Mapping of deformed fluvial terraces is based on a 30 m resolution Shuttle Radar Topography Mission (SRTM) Digital Elevation Model (DEM) (Figure 3). Additionally,

criteria include surface characteristics such as surface roughness, geomorphic, landforms, and terrace elevations to differentiate between terraces. Generally, all terraces exhibit smooth topography. Specifically, the two surfaces sampled for this study do not display bar and swale topography. Terraces at lower elevations, ~10m above the active river, show uneven bar and swale characteristics consistent with minimal surface erosion. Though we did not conduct rigorous soil testing, strong soil development was observed at site M1 and M2 (Qt3) (Figure 3). Field observations from the hand dug pits as well as road cuts aided in choosing sampling sites, avoiding buried soils or contacts between a fill and cut terrace. All TCN depth profile sampling was done in fill sediments. Pedogenic carbonate was not detected on any surfaces, consistent with minimal stripping of the surface. Cobble sized clasts were present at the surface of both sites. Medina 1 (480 m) has a lower elevation than Medina 2 (519 m), and thus these surfaces were originally mapped as different terraces.

Surface elevation data was collected on both terraces with submeter vertical accuracy using a Trimble® Geo 6000 GeoXT® Handheld device. Post-processing was conducted using a permanent station in Bogota to reduce vertical errors. The surface elevations collected in the field are identical to the SRTM 30 m DEM (4 m precision at 1σ) within error. Elevation data for the active river was not collected in the field because the river was inaccessible. SRTM DEM values are in agreement with the surface elevations collected in the field, therefore we are confident using only the elevation values derived from the DEM for the Humea River. Terrace elevations and the Humea river are projected onto a single line (Figure 4a), allowing net incision to be calculated at each elevation point of the terraces (Figure 4b).

3.2 Terrace geochronology

Two terraces (Figure 3) located in the hanging wall of the Guaicaramo thrust were sampled and dated for in situ ^{10}Be TCN surface exposure ages using the depth profiling method. ^{10}Be cosmogenic nuclides are formed by nuclear interactions between incoming galactic cosmic rays with ^{16}O and ^{28}Si in quartz sand found in young (10 to 100,000 years) sediments (Gosse, 2012; Gosse and Phillips, 2001). The abundance of TCNs in the uplifted terraces are proportional to the surface exposure age of the landform and reflects the time at which that terrace was uplifted by thrust faulting and abandoned by the river. Nuclide concentrations, however, can be influenced by inherited nuclides in the mineral of interest accumulated during sediment transport prior to final deposition. Because inheritance is likely to be non-zero (Gosse, 2012; Gosse and Phillips, 2001), we have used the depth profile method (Anderson et al., 1996; Hidy et al., 2010).

Sample locations were identified via remote sensing and field observations. Depth profile pits at the two sites were hand dug up to 1.5 – 2 m deep. Five samples, approximately 6-7cm thick, were collected below the soil mixing zone from each site to avoid vertical mixing. See Table 1 for sample depths. The pit at Medina 1 contained large clasts (cobbles to boulders up to 70cm diameter). Bioturbation was present, though it was not prevalent below the mixing zone. The Medina 2 pit exhibited large clasts (cobbles to small boulders up to 50cm diameter). A higher amount of bioturbation was present; the root system reached below the mixing zone. In both pits, rubification of the sediments was evident. No ash layers or buried soil horizons were visible, and there was no obvious change in lithology with depth.

From the ~2kg collected per sample we used grain sizes ranging between 250-1000 μm, extracting 4-15 g of pure quartz per sample. Physical and chemical sample treatment was done at PRIME Laboratory at Purdue University following the procedures outlined in Gosse and Phillips (2001). After separation of the target nuclide, the concentrations were measured using Accelerator Mass Spectrometry (AMS) at PRIME Laboratory.

3.3 Quaternary shortening calculation

The terrace and stream profiles are projected onto cross-section A-A' (Figure 6a). The cross-section modified from Silva (2010) is interpreted from seismic line MVI-1097. Fault geometry of the GT is further constrained by surface exposures, as well as published cross-sections and seismic reflection profiles (Mora et al., 2008; Mora et al., 2010). We reconstructed the uplifted terraces by backslipping the GT to restore the terraces to the Humea River elevations using 2D Move™ software from Midland Valley Exploration. The fault parallel flow algorithm was used for the reconstruction, following line length balancing principles (Dahlstrom, 1969; Egan et al., 1997; Egan et al., 1999). Cross section balancing also takes into account a deposition rate of 0.2 mm/yr (Parra et al., 2010). Following these principles, we calculated total shortening.

3.4 Topography and stream channel indices

Taking into account the methodologies described above, it is important to place the observed local deformation at Medina into a broader regional context. We have done this by studying the topography of the EC using stream channel profiles. The EC is

characterized by high elevations and relief. The Sierra Nevada del Cocuy represents the highest elevations of ~6500 m (Idárraga-García and Romero, 2010). To the south, the Bogotá Basin is situated at ~2500 m (Mora et al., 2008). The Llanos basin to the east ranges between 200-500 m. Though relief provides a general proxy for uplift, a more powerful tool to understand the variability of tectonic uplift of an orogen is to analyze the fluvial network. The fluvial network maintains a connection to the tectonic forcing and thus can be used to extract information about tectonic uplift. Channel longitudinal profiles therefore can provide quantitative analysis of the geomorphic response to uplift.

Quantifying fluvial morphometric parameters is based on the power-law scaling relationship between stream gradient (S) and drainage area (A) to determine the channel steepness index (k_s) (Flint, 1974):

$$S = k_s A^{-\theta} \quad (1).$$

However, this equation does not allow for comparison of k_s between streams with varying concavity values, which is a proxy for discharge. Therefore, a normalized channel steepness index (k_{sn}) can be calculated using a reference concavity (θ_{ref}),

$$k_{sn} = SA^{\theta_{ref}} \quad (2),$$

which can be directly compared between streams of varying concavity and drainage areas as a metric of relative channel steepness. The reference concavity value is based on analysis of streams in steady-state landscapes across orogens that all fall between 0.4 and 0.6 (Kirby and Whipple, 2001; Snyder et al., 2000; Wobus et al., 2006). Here, we have calculated k_{sn} using $\theta = .45$. Though normalized channel steepness analysis is most powerful when coupled with ^{10}Be catchment wide erosion rates (Cyr et al., 2010, 2014),

it can also be a useful metric in understanding first order uplift patterns across active orogens (Kirby and Whipple, 2012; Wobus et al., 2006).

Here we present the results from the eastern foothills of the EC for an area along strike of approximately 200 km. Steepness values were extracted from 30 m resolution topographic data with computational codes published from Geomorphtools.org following the procedures in Whipple et al. (2007). A more detailed explanation can be found in the supplementary materials. Normalized channel steepness values were calculated from the stream headwaters to the range front. This allowed for the values to be calculated only for the detachment limited portion of the streams. Values of k_{sn} become less reliable through alluvium, as streams can respond to uplift with a change in channel width or sinuosity and therefore not reflect an accurate k_{sn} value to evaluate (Wobus et al., 2006). These end points are user picked, so there is some variation; however, an effort was made to calculate values for only the bedrock portion of the streams.

4. Results and Discussion

4.1 Terrace geochronology

The modern Humea River flows perpendicular to the structural grain of the EC. The river is assumed to keep pace with tectonic uplift and represents the initial condition and underformed geometry for the uplifted and incised terraces. Thus, the terraces serve as Quaternary strain markers for quantifying deformation (Amos et al., 2007; Lavé and Avouac, 2001). The surface exposure ages of the 2 sites do not follow the expected trend of higher concentrations equating to older age of abandonment. This discrepancy,

however, can be resolved by understanding the fault geometry, which we discuss in more detail in section 4.2. In fact, Quaternary geochronology results indicate that the two sites are statistically the same age. Site specific production rates were calculated using the CRONUS Earth ^{10}Be calculator using Stone (2000) and Lal (1991). Age results are given below and the complete modeling results are presented in Table 2. Modal ages and maximum and minimum values are reported to 2σ, with a 3.5σ error required on the sample concentrations. The surface abandonment ages for sites M1 and M2 are 122^{+73}_{-4} ka and 117^{+83}_{-6} ka (Figure 5).

Modeling the profiles with all 5 samples yielded no results at a reasonable uncertainty. Difficulties in the depth profile modeling can be due to several reasons, including inconsistent inheritance (likely due to mixing at time of deposition); unrecognized bioturbation resulting in vertical mixing; and error in sample chemistry or AMS measurements (Mercader et al., 2012). Therefore, the uppermost sample at each location was excluded from analysis as we believe they were located in the lowermost section of the mixing zone and therefore have experienced vertical mixing from their original depositional position. Even with the removal of the uppermost sample, uncertainty on the profile fits could not be lowered beyond 3.5σ error on the concentrations. Furthermore, it is likely the terraces experienced low erosion rates during surface exposure followed by a period of aggradation and a final continued period of erosion. This is deduced from the modelling, which required lower neutron attenuation lengths in order to achieve any results. In a rapidly aggrading surface, the attenuating length decreases as the sediments become buried. The full set of parameters used can be found in the supplementary materials.

The inheritance values also provide insight into the paleoerosion history of the basin. Low TCN inheritance values indicate the grains were exposed for a shorter duration during their transport history prior to deposition at the terrace. Grains sourced from convex or steep slopes yield low TCN concentrations, while gently sloping landscapes yield higher concentrations. Furthermore, if sediment is sourced from higher altitudes we would expect the inheritance to be higher, as TCN production increases with altitude (Gosse, 2012). Medina 1 and Medina 2 have low inheritance values, therefore, the low inheritance values indicate high catchment erosion rates. In this region, the high erosion rates are likely due to glaciation in the upper portion of the catchments. The timing of fluvial terrace abandonment is consistent with the end of marine isotope stage 6 (Imbrie et al., 1984). With the age of the terrace, incision and shortening rates are constrained in the following section.

4.2 Incision rates

Figure 4a shows the projection of the topographic profiles of the two terraces and Humea River, on to a section perpendicular to the strike of the Guaicaramo thrust. We calculated the net incision by subtracting elevations of the Humea River from the terrace elevations (Figure 4b). Terrace elevations were measured in the field with submeter accuracy and the river were determined from the 30 m DEM, calculated with a normally distributed error of 4 m (1σ) as outlined in section 3.1. Here we report total incision and incision rates with 2σ error. Maximum incision values for the two sites are Medina 1: 67 ± 6.6 m, and Medina 2: 131 ± 6.6 m. We calculated incision rates using the full distribution

of ages. Medina 1: 0.66 ± 0.1 mm/yr; 1.12 ± 0.22 mm/yr. The weighted average of the incision rates is: 0.74 ± 0.09 mm/yr.

The observed patterns of incision are easily reconciled with an understanding of the fault geometry, which in this case is a listric thrust (Figure 6). Site M1 is located on a hanging wall flat on footwall flat geometry and therefore we expected greater horizontal movement. Site M2 is closer to the fault tip in the foreland and is located on a hanging wall flat on footwall ramp where the thrust cuts up section. Consequently, site M2 has experienced greater vertical movement (Figure 4). The terrace profiles and fault geometry are next used to reconstruct the slip history on the Guaicaramo thrust.

4.3 Shortening rates

Section balancing takes into account a 0.2 mm/yr sedimentation rate (Parra et al., 2010). Results of section balancing show that a minimum of 220 ± 22 m (2σ) is required to reconstruct the deformed terraces (Site M2) to the present elevation of the Humea river (Figure 6b). An additional 60 m for a total of 280 ± 28 m is required to reconstruct site M1 (Figure 6c). From the modeling, there is no indication of slip along the backthrust and none is required to reconstruct the deformed terraces back to the modern stream. Because the terraces are located on the lateral termination of the backthrust, this is not unexpected. We imposed a 10% error on the amount of shortening. Shortening rates presented below were calculated by using the age of the respective terrace and the total amount of shortening. Calculated slip rate for site M1 and M2 is 1.93 ± 0.44 mm/yr (2σ) and 1.54 ± 0.40 mm/yr (2σ), respectively. The weighted mean Quaternary slip rate is 1.72 ± 0.30 mm/yr.

Though sites M1 and M2 are the same age, the total amount of slip required in the section balancing varies by 60 m. This does not translate to statistically significant differences in the calculated shortening rate. We propose a slip gradient along the fault to account for the differences in shortening needed to reconstruct Medina 1 (250m) and Medina 2 (200m). We do not model or propose internal shearing in the section balancing, however, the observed differences in slip rates could be due to a slip gradient as is commonly observed during seismic events. Specifically, we would observe the greatest slip along the flat on flat. Less slip occurs along the shallower, listric portion of the fault toward the fault tip.

4.4 Normalized steepness and concavity

From the topographic data we have extracted k_{sn} values for the entire EC (Figure 7). These data are noisy; however, some patterns are observed with high k_{sn} values present in the western and eastern flanks of the EC, though with a greater concentration along the eastern flank. The northern region of the EC also exhibits a high density of large k_{sn} values. From the individually selected streams on the eastern flank k_{sn} values range between 10 and 500 (Figure 8a). A single mean k_{sn} value was calculated for the primary streams draining the EC. It is necessary to calculate the values for the detachment limited portion of the streams only, as continuing the calculations into the Llanos basin suppressed the mean by various processes as previously explained in section 3.4. Mean values are consistent for most of the southern and central portion of the EC and increases in the northern portion (Figure 8b). Mean k_{sn} values range from ~130 in the south to ~280 in the northern foothills. These values are then compared to recent shallow (< 70 km)

seismicity in the region (Figure 8b). The EC is seismically active and large events have occurred along the entire stretch of the EC. Though no strong correlation between k_{sn} and seismicity are observed, we can however, make some first order observations. In the north, where we see the highest k_{sn} values, we can see a greater number of events as well as deeper earthquakes. Thus indicating that the observed patters of k_{sn} are in response to active mountain building events.

While mean values generally increase to the north, high k_{sn} values are also observed along stream segments of the southern streams (Figure 8). We posit that this may be due to the precipitation gradients observed along the Llanos foothills, as precipitation increases to the South (Mora et al., 2008). Higher precipitation could increase the k_{sn} values in a portion that is experiencing lower magnitude uplift. Lithologic variability could also explain the discrepancy; however, no obvious contact relationships are observed when comparing k_{sn} values with the geologic units and no detailed field mapping of lithology and more importantly rock strength was conducted. Lateral stream offsets do coincide with fault locations in some areas, particularly in the south-central region (Figure 8a).

Normalized steepness indices for the Colombian subandes are consistent with high uplift rates and are comparable with mountain ranges worldwide (Kirby and Whipple, 2012). Safran et al. (2005) observed k_{sn} values ranging from 200-600 for most of the catchments analyzed in the Bolivian Andes. In the San Gabriel Mountains, DiBiase et al. (2010) found streams with ksn values ranging from <100 to 200. Ouimet et al. (2009) quantified k_{sn} in Eastern Tibet with values ranging from 100-450. In contrast, Bellin et al. (2014) presented k_{sn} values in the Spanish Beltic Cordillera, which experiences low uplift

rates (<200 mm/ka) and proportionally low mean catchment k_{sn} values between 9.6 and 75.6 and a regional mean value of 31.5 ± 19.4. Values from the Appalachian mountains from Miller et al. (2013) range between 15 and 45.

5. Regional Implications

5.1 Regional shortening, deformation style, and seismic hazards

The current orientation of maximum horizontal stress in the EC is favorable for Cenozoic reactivation of Mesozoic normal faults. Thus, as the orogen has reached super critical conditions, it has advanced eastward along these pre-existing weaknesses (Mora et al., 2010; Parra et al., 2009; Veloza et al., 2015). The northern portion of the Guaicaramo thrust represents one of many inverted rift features; however, the area studied here exhibits a thin skinned flat detachment style that is inconsistent with an inverted half-graben (Mora et al., 2013; Tesón et al., 2013). Thus the orogenic thrust is not only advancing along pre-existing features, but also through thin-skinned thrust faulting structurally above the crystalline basement.

Our observations in Medina reflect the effect of a listric fault geometry on surface deformation and landscape evolution. With increasing proximity to the fault tip, we observe greater vertical uplift where the GT cuts up-section. We demonstrate, based on the surface abandonment ages of two fluvial terraces, topographic profiles, and fault geometry that the Quaternary shortening rate of the Guaicaramo thrust is 1.72 ± 0.30 mm/yr. Likewise, our results indicate that the northernmost extent of the backthrust has not caused significant slip. These slip rate results are lower than the geodetic horizontal

velocities of 2.5 mm/yr (Trenkamp et al., 2002). One reason for this discrepancy is the effect of the seismic cycle (Friedrich et al., 2003; Tapponnier et al., 2001; Youngs and Coppersmith, 1985). The geologically derived slip rates encompass several seismic cycles, in contrast to the instantaneous geodetic rates. The GPS rates indicate they might be responding to recent events and thus overestimating long-term slip rates. Furthermore, coseismic movement might have also occurred with an opposite sense of deformation from the interseismic and millennia-scale slip rates.

Another possibility is that the Servitá fault to the west and smaller frontal thrusts to the ESE (Mora et al., 2013) also accommodate active shortening. Understanding the differing characteristics and slip rates along strike are important for determining where the greatest seismic hazards lie. In the north, where faulting is basement involved, strain is localized on a single active fault (Mora et al., 2006; Veloza et al., 2015). To the south, deformation is distributed along thin skinned sections of the thrust belt such as the GT. Thus, earthquakes can nucleate along several active strands. This suggests larger events are more likely to occur in the north, posing the greatest risk.

Nonetheless, using the geologically derived slip rate we estimate the contribution of the GT to the total shortening budget across the northern Andes using 58 mm/yr as the convergence rate between the Nazca and South American plates (Trenkamp et al., 2002). We estimate that this portion of the Guaicaramo thrust represents ~3% of the total horizontal shortening across the Colombian Andes, which was previously unknown. In contrast, the work of Veloza et al. (2015) show that the northern portion of the EC at the Tame anticline is accommodating 2-6% of the total shortening across the northern Andes.

6. Conclusions

Our results provide key insights into the neotectonic deformation of the EC of Colombia. The work presented in this paper has three main contributions: (1) our results underscore the importance of constraining fault geometry in order to understand its effect on the geomorphic evolution of an active thrust belt. In the case of the Medina sites which are deformed by a listric fault, the magnitude of vertical uplift is greatest near the fault tip where the geometry is a hanging wall flat on footwall ramp. (2) This study presents novel analyses for the region. Using k_{sn} as another tool to quantify geomorphic indices of tectonic uplift, we have characterized first order features of active deformation of the Colombian subandes and the EC. This study serves as a foundation for further studies to compare basin erosion rates with k_{sn} values. (3) This work represents the first quantification of Quaternary slip rates for the southern EC of Colombia, filling in an important gap between our understanding of long term deformation rates and geodetic rates. Identifying which faults are accommodating the most slip is crucial in characterizing the neotectonic development of the EC, ultimately gaining insight into the rate of thrust front advancement.

Acknowledgements

KU Department of Geology, AAPG Foundation, and the Kansas Geological Foundation provided financial support to Erica Dalman. Ecopetrol also provided support to M.Taylor. This manuscript greatly improved from discussions with John Gosse and Alan Hidy regarding the TCN modeling. We would also like to thank Eliseo Tesón for his

help with the fault reconstruction, done using a software grant from Midland Valley Exploration (Move™).

Figures

Figure 1

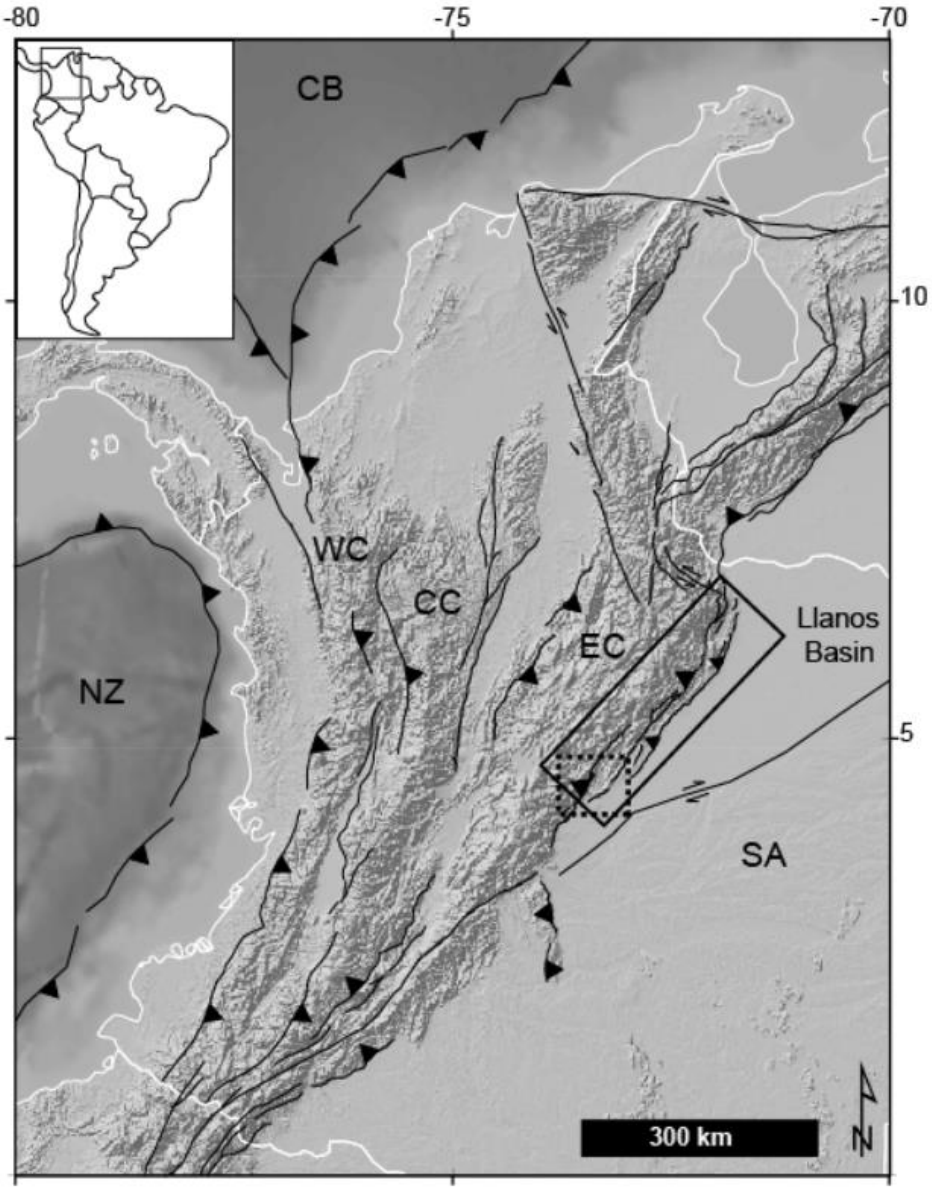

Figure 1. Digital Elevation Model of the Colombian Andes and tectonic features. Fault locations from Veloza et al. (2012). CB: Caribbean plate; SA: South American plate; NZ: Nazca Plate; EC: Eastern Cordillera; CC: Central Cordillera; WC: Western Cordillera. The inset map highlights the location of Figure 1. The solid rectangle shows the location of Figure 2, 8, and 9. The dashed rectangle highlights the location of Figure 3.

Figure 2

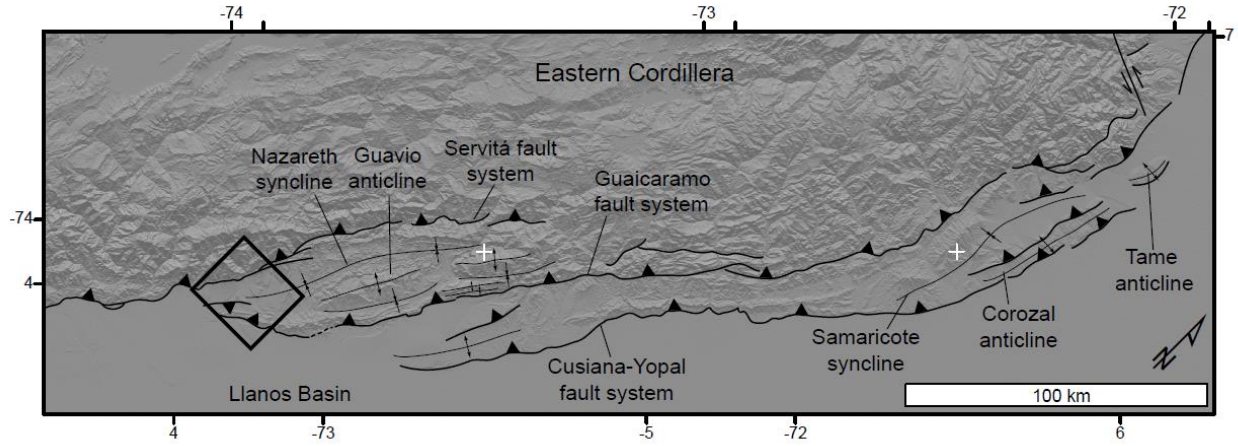
-74
-73
-72
-7
Eastern Cordillera
Nazareth syncline
Guavio anticline
Servitá fault system
Guaicaramo fault system
Tame anticline
Corozal anticline
Samaricote syncline
Cusiana-Yopal fault system
Llanos Basin
100 km
-74
4
4
-73
-5
-72
6

Figure 2. Digital Elevation Model of the EC foothills between ~4° and 6° N, modified from Mora et al. (2010) and Veloza et al. (2015). The black rectangle highlights the location of Figure 3.

Figure 3

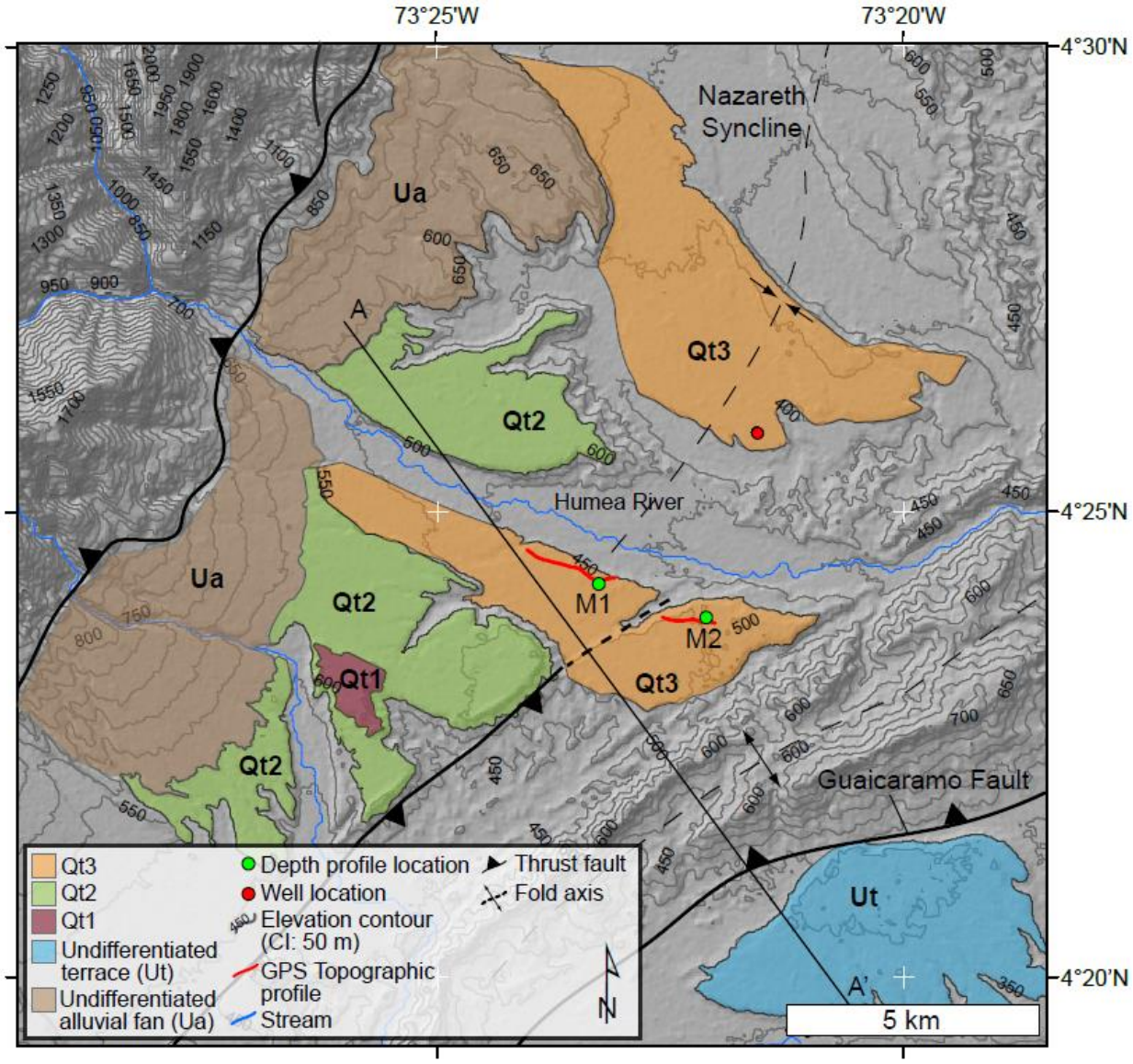
73°25'W
73°20'W
4°30'N
4°25'N
4°20'N
Nazareth
Syncline
Ua
Qt3
Qt2
Humea River
M1
M2
Qt1
Guaicaramo Fault
Ut
A
A'
5 km
N
Qt3
Qt2
Qt1
Undifferentiated terrace (Ut)
Undifferentiated alluvial fan (Ua)
Depth profile location
Well location
Elevation contour (CI: 50 m)
GPS Topographic profile
Stream
Thrust fault
Fold axis

Figure 3. Shaded relief map created from a 30m SRTM DEM. Line A-A' indicates the location for Figure 5. Two deformed terraces (M1 and M2) were sampled for ^{10}Be depth profiles. Fault locations from Mora et al. (2010) and Veloza et al. (2012).

Figure 4

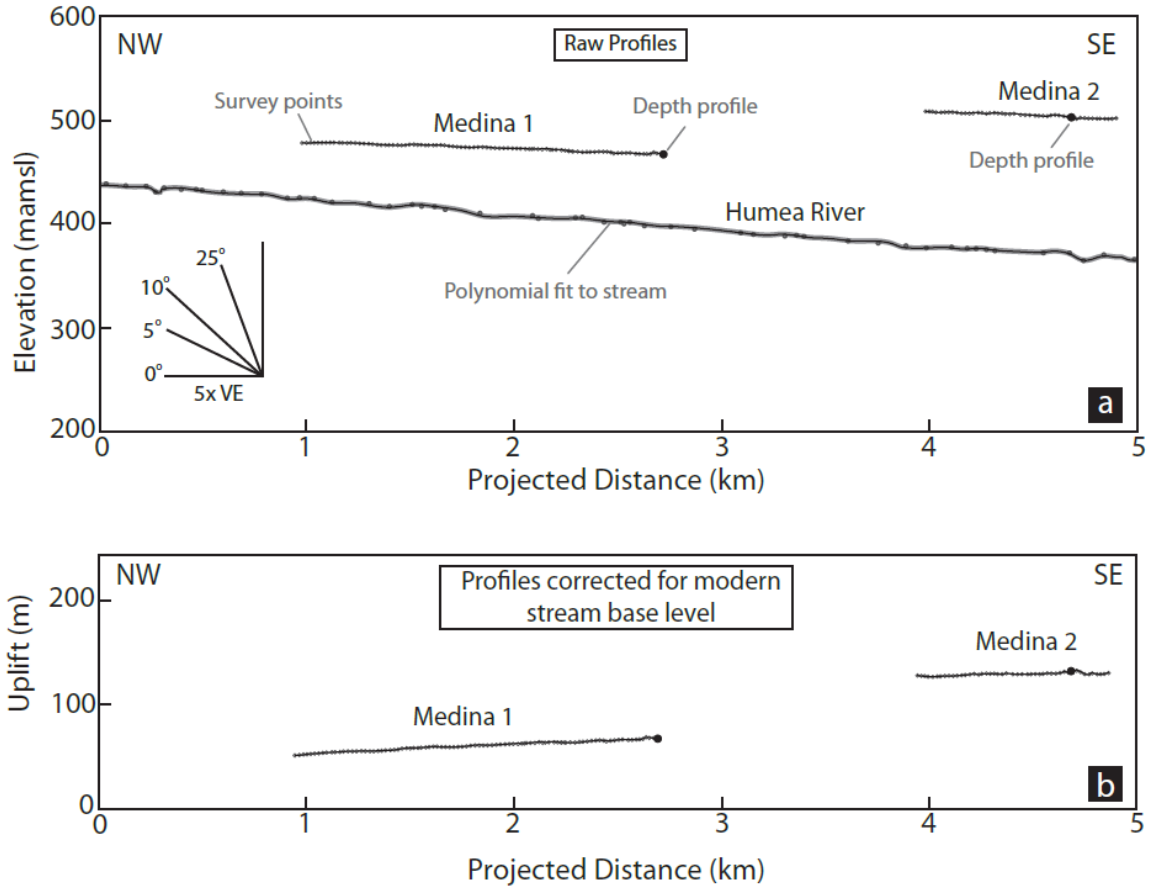
NW
Raw Profiles
SE
Survey points
Medina 1
Depth profile
Medina 2
Depth profile
Humea River
Polynomial fit to stream
25°
10°
5°
0°
5x VE
Elevation (mamsl)
600
500
400
300
200
0
1
2
3
4
5
Projected Distance (km)
a
NW
Profiles corrected for modern stream base level
SE
Medina 2
Medina 1
Uplift (m)
200
100
0
0
1
2
3
4
5
Projected Distance (km)
b

Figure 4. Terrace and stream elevations projected onto a profile that is perpendicular to the fold axis. See Figure 2 for map location. A) Raw terrace and Humea River elevations. Terrace elevations are from GPS data collected in the field, open circles show survey locations. Black circles indicate ^{10}Be depth profile sample locations. Humea River elevations are derived from the 30m DEM. Elevation points are shown with the dots, the shaded area represent the 4m (1σ) uncertainty. B) Net uplift of deformed terraces.

Figure 5

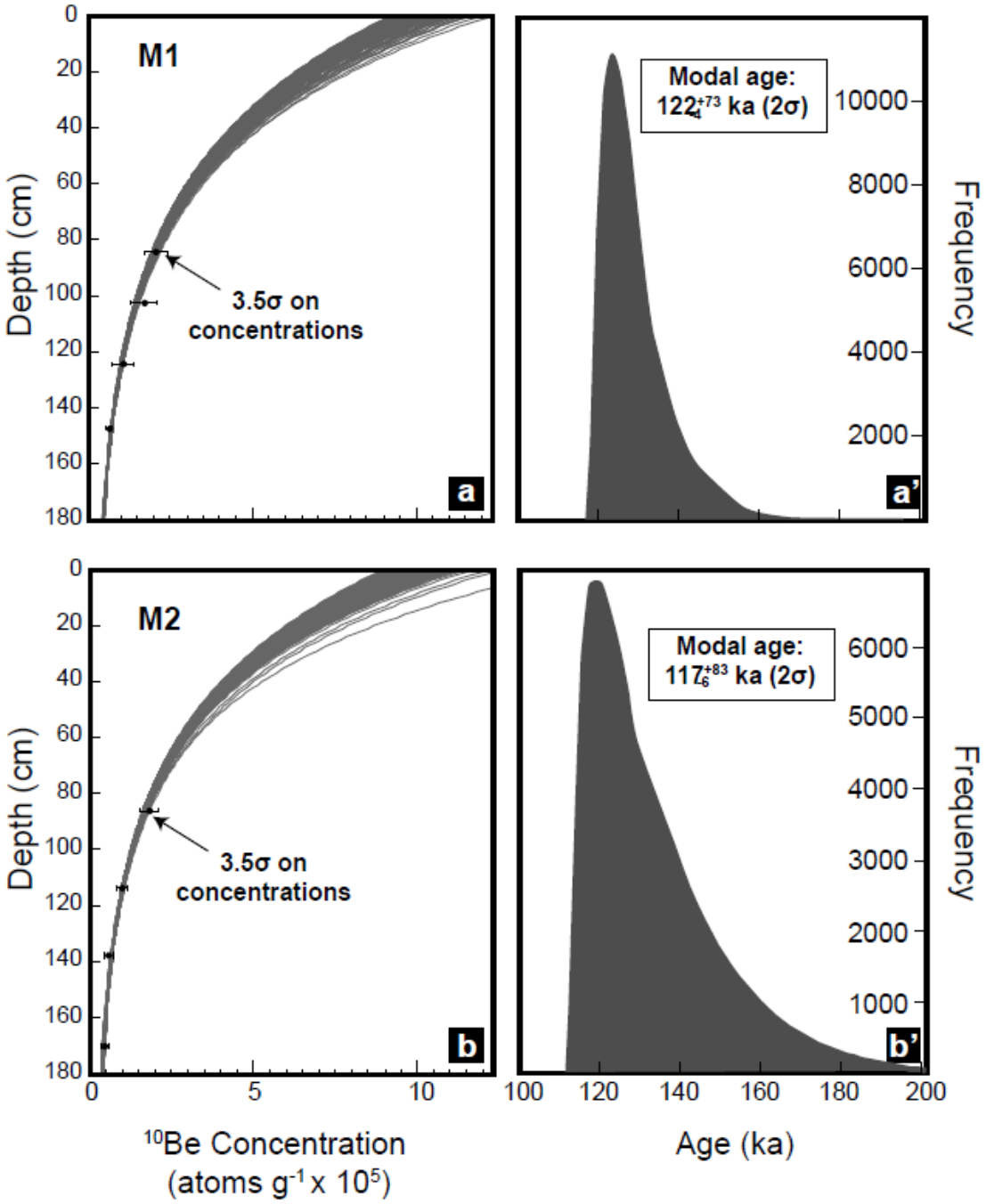
M1
Depth (cm)
3.5σ on concentrations
a
Modal age: 122 +73 -4 ka (2σ)
Frequency
a'
M2
Depth (cm)
3.5σ on concentrations
b
Modal age: 117 +83 -6 ka (2σ)
Frequency
b'
10Be Concentration (atoms g-1 x 10^5)
Age (ka)

Figure 5. ^{10}Beryllium concentration versus depth profiles for sites M1 (a) and M2 (b) and age distribution histograms (a') and (b'). Concentration measurements are shown with 3.5σ error. Solutions shown in shaded area to 2σ after 100,000 iterations of the Monte Carlo simulation v.1.2 Hidy et al. (2010). Modal ages and maximum and minimum values are reported in (a') and (b').

Figure 6

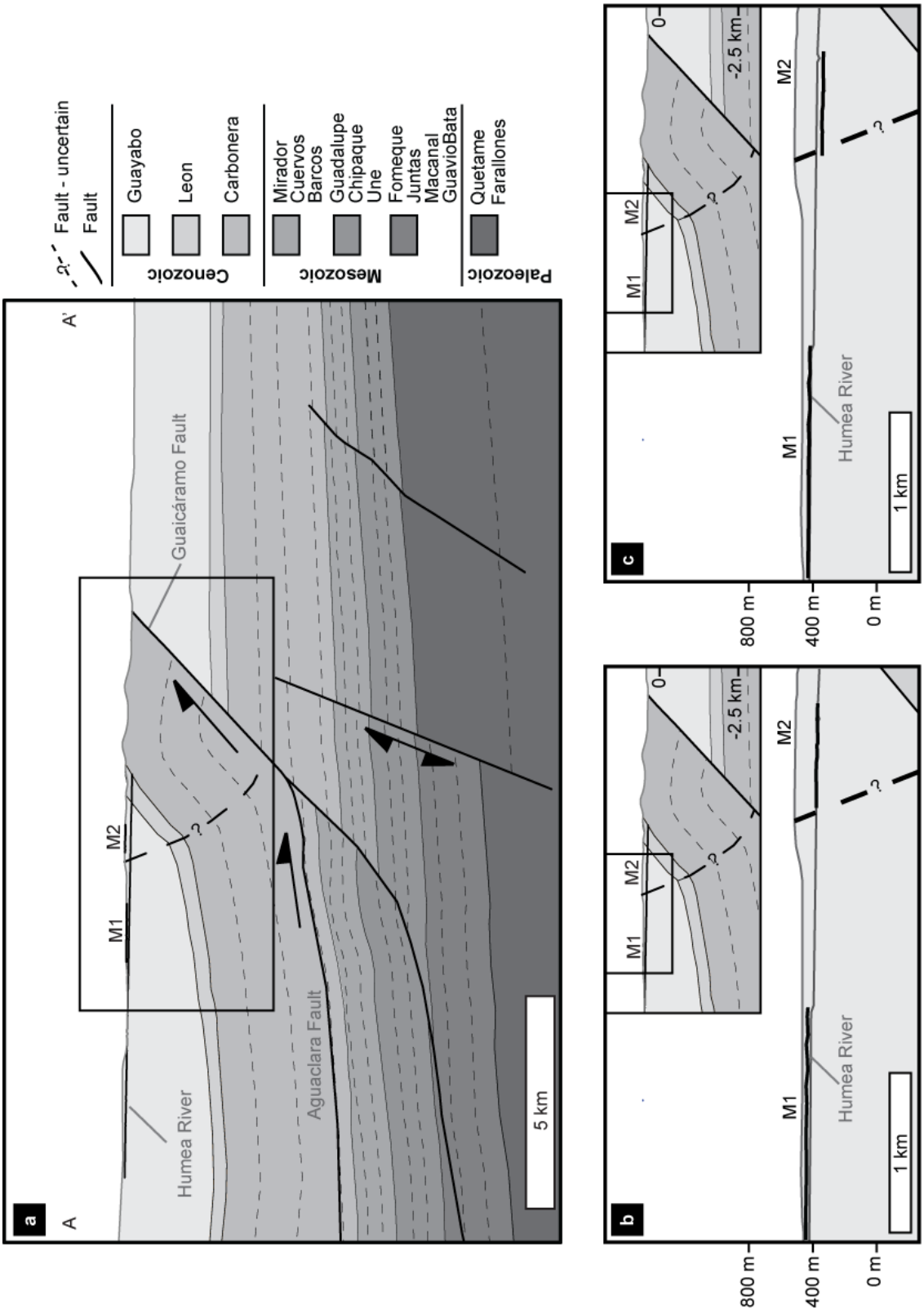
Fault - uncertain
Fault
Cenozoic
Guayabo
Leon
Carbonera
Mesozoic
Mirador
Cuervos
Barcos
Guadalupe
Chipaque
Une
Fomeque
Juntas
Macanal
GuavioBata
Paleozoic
Quetame
Farallones
a
A
A'
Guaicáramo Fault
Aguaclara Fault
Humea River
M1
M2
?
5 km
b
c
0
-2.5 km
800 m
400 m
0 m
1 km

Figure 6. Schematic solutions from shortening calculations. Fault slip reconstructions done using 2D Move software. All balancing was done using the fault parallel flow algorithm (Egan et al., 1997; Egan et al., 1999). Two solutions of restoration of the deformed terraces to the undeformed base level (Humea River) are presented. Inset cross-sections show initial condition. A) Cross-section modified from Silva (2010), interpreted from seismic line MVI-97-1070. See Figure 3 for location. Topography (gray line) derived from a 30m DEM. M1- Medina 1; M2 – Medina 2. B) Minimum shortening of 220 ± 22 m restores M2 to undeformed base level. C) Results from 280 ± 28 m backslip along the Guaicaramo thrust (GT). M1 is restored to undeformed base level.

Figure 7

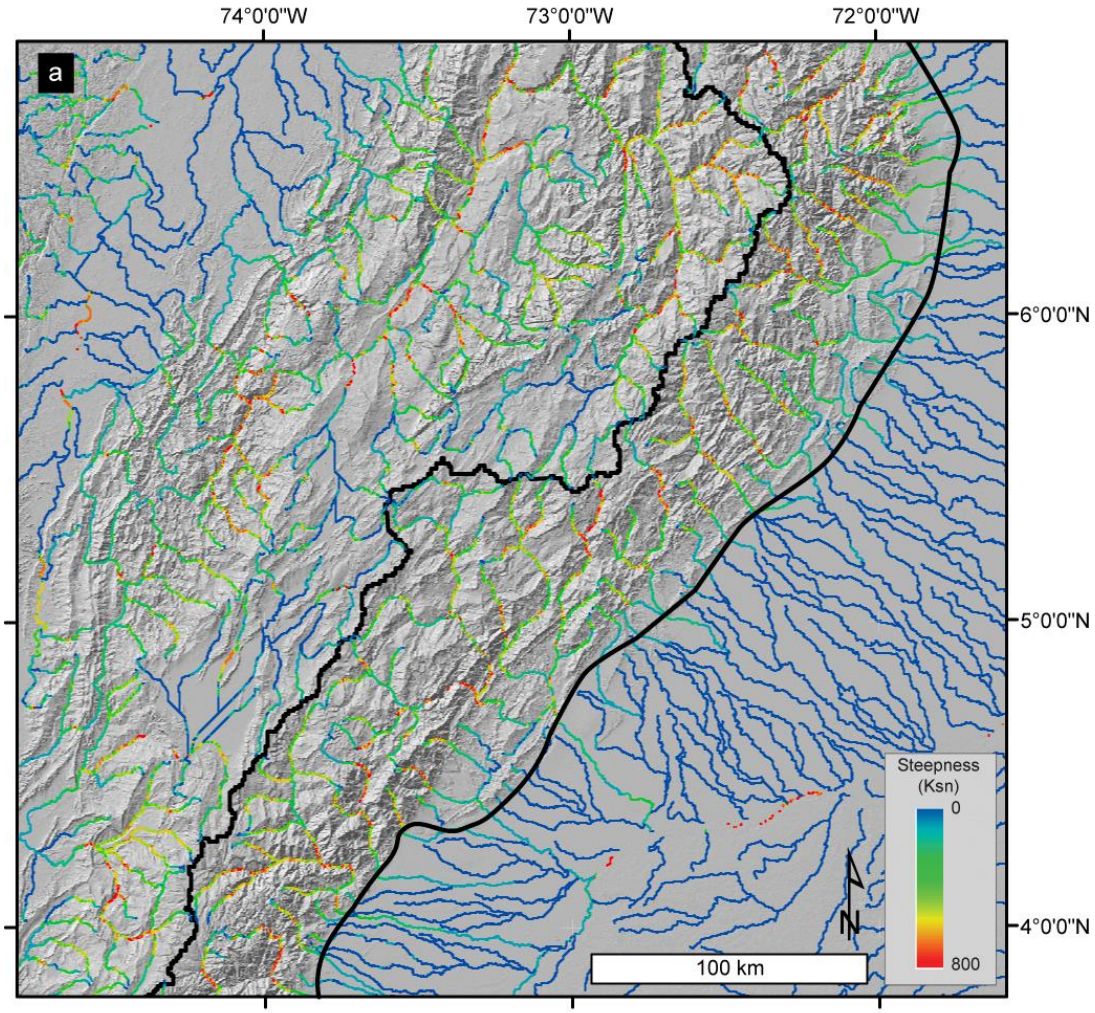
74°0'0"W
73°0'0"W
72°0'0"W
6°0'0"N
5°0'0"N
4°0'0"N
a
Steepness (Ksn)
0
800
N
100 km

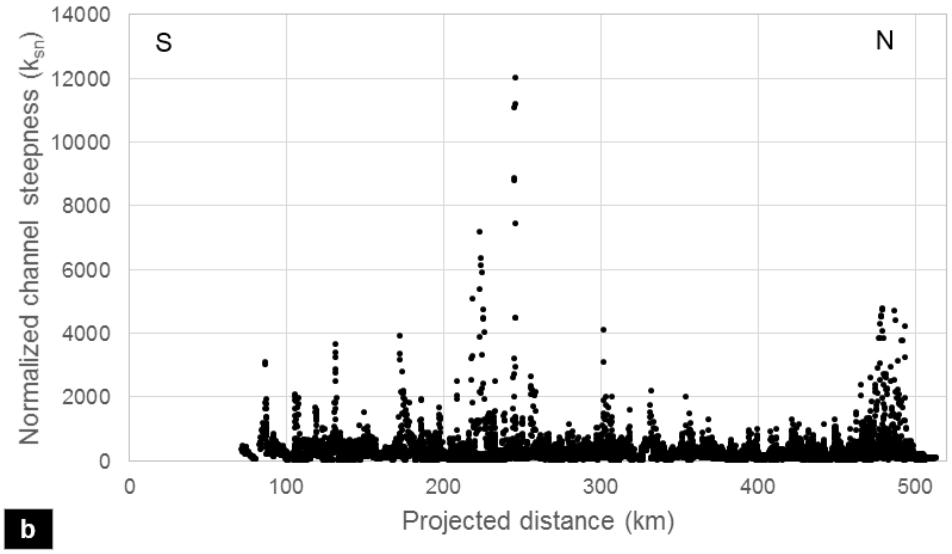
S
N
Normalized channel steepness (k_{sn})
14000
12000
10000
8000
6000
4000
2000
0
0
100
200
300
400
500
Projected distance (km)
b

Figure 7. A) Normalized channel steepness (k_{sn}) for the EC foothills. See Figure 2 for location. Data extracted from a 30m DEM using MATLAB codes available at geomorphtools.org. K_{sn} is defined from a regression of Ks along individual slope-area segments using θ_{ref} (reference concavity). $K_{sn} = k_s A_{cent}^{(\theta ref - \theta)}$; $A_{cent} = 10^{(\log A_{max} + \log A_{min})/2}$. High k_{sn} values are observed throughout the entire EC. B) K_{sn} values for the eastern flank (within black polygon) projected onto a single line.

Figure 8

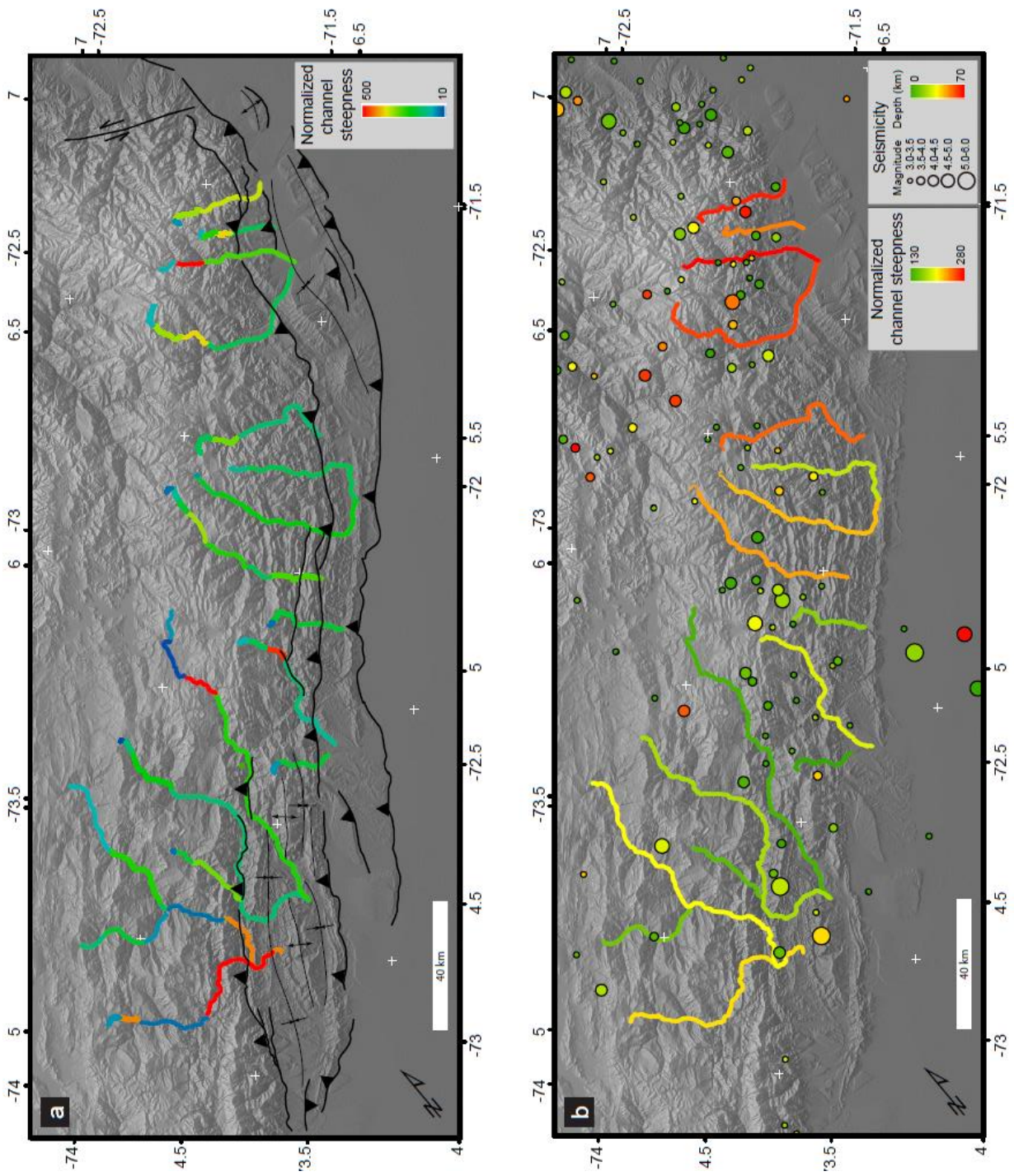
a
Normalized channel steepness
500
10
40 km
b
Seismicity
Magnitude
Depth (km)
3.0-3.5
3.5-4.0
4.0-4.5
4.5-5.0
5.0-6.0
0
70
Normalized channel steepness
130
280
40 km

Figure 8. Normalized channel steepness (k_{sn}) for the Eastern Cordillera foothills. Streams and data limit were user defined using $\theta_{ref} = 0.45$. See Figure 2 for location A) K_{sn} values are generally constant in the central portion. Highest values are in the north and a portion in the south. The high values observed in the south are likely due to large amounts of precipitation. B) Mean normalized channel steepness (k_{sn}) and recent shallow seismicity (RSNC, 2015). Mean ksn generally increase to the north.

Table 1

Summary Of Sample Data from sites Medina 1 (M1) and Medina 2 (M2)[a]

Sample ID	Location (°N/°W)	Depth (cm)	Thickness (cm)	Grain Size Range (μm)	Dissolved Mass (g)	Be Carrier Mass[b] (g)	Corrected 10Be/9Be	10Be concentration (atoms/g)	10Be concentration - blank subtracted (atoms/g)	1σ AMS Error (%)	1σ Total Measured Error (%)
1	4.40433/73.38489	144	7	250-1000	20.651	0.2508	7.91778E-14	68700	65941	4.60%	5.60%
2	4.40433/73.38489	121	7	250-1000	4.022	0.2495	2.72416E-14	120734	106568	8.50%	9.40%
3	4.40433/73.38489	99	7	250-1000	3.419	0.2498	3.59922E-14	187876	171211	6.50%	7.40%
4	4.40433/73.38489	81	7	250-1000	4.837	0.2482	6.00541E-14	220160	208380	5.40%	6.30%
5	4.40433/73.38489	50	6	250-1000	13.513	0.2493	1.70868E-13	225217	221000	3.20%	4.40%
6	4.39709/73.374	167	7	250-1000	18.212	0.2507	5.21735E-14	51311.658	48183	6.20%	7.10%
7	4.39709/73.374	135	6	250-1000	28.273	0.2496	9.88561E-14	62351.306	60336	5.60%	6.40%
8	4.39709/73.374	111	6	250-1000	18.685	0.2492	1.09253E-13	104101.67	101052	4.00%	5.10%
9	4.39709/73.374	83	6	250-1000	9.474	0.25	1.0056E-13	189583.82	183570	4.20%	5.20%
10	4.39709/73.374	50	6	250-1000	8.698	0.2472	1.11944E-13	227299.91	220749	4.30%	5.30%

[a]All samples run at PRIME Laboratory, Purdue University

[b]Carrier concentration 1069 ppm

Table 1 Summary Of Sample Data from Medina Sites 1 and 2 Formatted According to Frankel et al. (2010).

Table 2

Table 2

^{10}Be depth profile simulation results[a]

Site name	Age (ka)	Inheritance (10^4 atoms g-1)	Erosion Rate (cm ka-1)
M1			
Mean	129.3	0.13	-0.62
Median	127.2	0.1	-0.64
Mode	122.7	0.01	-0.69
Lowest χ^2	128.8	0.01	-0.7
Maximum	195.2	0.96	-0.28
Minimum	118	0	-0.7
Bayesian most probable	122.4	0	-0.7
Bayesian 2σ upper	168.2	0.78	-0.26
Bayesian 2σ lower	111.7	NaN	NaN
M2			
Mean	132.3	0.27	-0.54
Median	127.8	0.21	-0.56
Mode	117.3	0.01	-0.69
Lowest χ^2	144.9	0.78	-0.52
Maximum	200	1	-0.2
Minimum	111.1	0	-0.7
Bayesian most probable	116.8	0	-0.69
Bayesian 2σ upper	172.1	0.85	-0.25
Bayesian 2σ lower	106.7	NaN	-0.7

[a] See Supplementary Figure 1 for all parameters used for each depth profile

Table 2 Statistics for the Simulation of two depth profiles. Maximum and minimum values represent the 95% (2σ) confidence window for each parameter.

References

Aggarwal, Y., Seismic slip rates and earthquake rupture zones in the southern Caribbean: implications for plate motions and earthquake hazard in this region, *in* Proceedings 10th Caribbean Geological Conference1983, p. 16.

Amos, C. B., Burbank, D. W., Nobes, D. C., and Read, S. A., 2007, Geomorphic constraints on listric thrust faulting: Implications for active deformation in the Mackenzie Basin, South Island, New Zealand: Journal of geophysical research, v. 112, no. B3, p. B03S11.

Anderson, R. S., Repka, J. L., and Dick, G. S., 1996, Explicit treatment of inheritance in dating depositional surfaces using in situ 10Be and 26Al: Geology, v. 24, no. 1, p. 47-51.

Bellin, N., Vanacker, V., and Kubik, P., 2014, Denudation rates and tectonic geomorphology of the Spanish Betic Cordillera: Earth and Planetary Science Letters, v. 390, p. 19-30.

Cazier, E., Hayward, A., Espinosa, G., Velandia, J., Mugniot, J., and Leel Jr, W., 1995, Petroleum geology of the Cusiana field, Llanos Basin foothills, Colombia: AAPG bulletin, v. 79, no. 10, p. 1444-1462.

Colmenares, L., and Zoback, M. D., 2003, Stress field and seismotectonics of northern South America: Geology, v. 31, no. 8, p. 721-724.

Cortés, M., Colletta, B., and Angelier, J., 2006, Structure and tectonics of the central segment of the Eastern Cordillera of Colombia: Journal of South American Earth Sciences, v. 21, no. 4, p. 437-465.

Cyr, A. J., Granger, D. E., Olivetti, V., and Molin, P., 2010, Quantifying rock uplift rates using channel steepness and cosmogenic nuclide–determined erosion rates: Examples from northern and southern Italy: Lithosphere, v. 2, no. 3, p. 188-198.

-, 2014, Distinguishing between tectonic and lithologic controls on bedrock channel longitudinal profiles using cosmogenic< sup> 10</sup> Be erosion rates and channel steepness index: Geomorphology, v. 209, p. 27-38.

Dahlstrom, C., 1969, Balanced cross sections: Canadian Journal of Earth Sciences, v. 6, no. 4, p. 743-757.

DeCelles, P. G., Ducea, M. N., Kapp, P., and Zandt, G., 2009, Cyclicity in Cordilleran orogenic systems: Nature Geoscience, v. 2, no. 4, p. 251-257.

DiBiase, R. A., Whipple, K. X., Heimsath, A. M., and Ouimet, W. B., 2010, Landscape form and millennial erosion rates in the San Gabriel Mountains, CA: Earth and Planetary Science Letters, v. 289, no. 1, p. 134-144.

Dimate, C., Rivera, L., Taboada, A., Delouis, B., Osorio, A., Jimenez, E., Fuenzalida, A., Cisternas, A., and Gomez, I., 2003, The 19 January 1995 Tauramena (Colombia) earthquake: geometry and stress regime: Tectonophysics, v. 363, no. 3, p. 159-180.

Egan, S., Buddin, T., Kane, S., and Williams, G., 1997, Three-Dimensional Modelling And Visualisation In Structural Geology: New Techniques For The Restoration And Balancing Of Volumes.: Electronic Geology 1, no. 7, p. 67-82.

Egan, S., Kane, S., Buddin, T., Williams, G., and Hodgetts, D., 1999, Computer modelling and visualisation of the structural deformation caused by movement along geological faults: Computers & Geosciences, v. 25, no. 3, p. 283-297.

EIA, U. S., 2014, Country Analysis - Colombia.

England, P., and Jackson, J., 2011, Uncharted seismic risk: Nature Geoscience, v. 4, no. 6, p. 348-349.

Flint, J., 1974, Stream gradient as a function of order, magnitude, and discharge: Water Resources Research, v. 10, no. 5, p. 969-973.

Frankel, K. L., Finkel, R. C., and Owen, L. A., 2010, Terrestrial cosmogenic nuclide geochronology data reporting standards needed: Eos, Transactions American Geophysical Union, v. 91, no. 4, p. 31-32.

Freymueller, J. T., Kellogg, J. N., and Vega, V., 1993, Plate motions in the North Andean region: Journal of Geophysical Research: Solid Earth (1978–2012), v. 98, no. B12, p. 21853-21863.
Friedrich, A. M., Wernicke, B. P., Niemi, N. A., Bennett, R. A., and Davis, J. L., 2003, Comparison of geodetic and geologic data from the Wasatch region, Utah, and implications for the spectral character of Earth deformation at periods of 10 to 10 million years: Journal of Geophysical Research: Solid Earth (1978–2012), v. 108, no. B4.
Gosse, J. C., 2012, Terrestrial Cosmogenic Nuclide Techniques for Assessing Exposure History of Surfaces and Sediments in Active Tectonic Regions: Tectonics of Sedimentary Basins, p. 63-79.
Gosse, J. C., and Phillips, F. M., 2001, Terrestrial in situ cosmogenic nuclides: theory and application: Quaternary Science Reviews, v. 20, no. 14, p. 1475-1560.
Gutscher, M.-A., Malavieille, J., Lallemand, S., and Collot, J.-Y., 1999, Tectonic segmentation of the North Andean margin: impact of the Carnegie Ridge collision: Earth and Planetary Science Letters, v. 168, no. 3, p. 255-270.
Helmens, K., 1988, Late Pleistocene glacial sequence in the area of the high plain of Bogotá (Eastern Cordillera, Colombia): Palaeogeography, Palaeoclimatology, Palaeoecology, v. 67, no. 3, p. 263-283.
Helmens, K., and Van der Hammen, T., 1994, The Pliocene and Quaternary of the high plain of Bogotá (Colombia): a history of tectonic uplift, basin development and climatic change: Quaternary International, v. 21, p. 41-61.
Hidy, A. J., Gosse, J. C., Pederson, J. L., Mattern, J. P., and Finkel, R. C., 2010, A geologically constrained Monte Carlo approach to modeling exposure ages from profiles of cosmogenic nuclides: An example from Lees Ferry, Arizona: Geochemistry, Geophysics, Geosystems, v. 11, no. 9.
Hooghiemstra, H., 1989, Quaternary and Upper-Pliocene glaciations and forest development in the tropical Andes: evidence from a long high-resolution pollen record from the sedimentary basin of Bogotá, Colombia: Palaeogeography, Palaeoclimatology, Palaeoecology, v. 72, p. 11-26.
Hooghiemstra, H., Wijninga, V. M., and Cleef, A. M., 2006, The paleobotanical record of Colombia: implications for biogeography and biodiversity 1: Annals of the Missouri Botanical Garden, v. 93, no. 2, p. 297-325.
Hoorn, C., 1994, An environmental reconstruction of the palaeo-Amazon river system (Middle–Late Miocene, NW Amazonia): Palaeogeography, Palaeoclimatology, Palaeoecology, v. 112, no. 3, p. 187-238.
Idárraga-García, J., and Romero, J., 2010, Neotectonic study of the Santa Marta Fault System, western foothills of the Sierra Nevada de Santa Marta, Colombia: Journal of South American Earth Sciences, v. 29, no. 4, p. 849-860.
IDEAM, 2012, Mapa de Temperatura Media Anual y Pisos Térmicos. República de Colombia: Instituto de Hidrología, Meteorología y Estudios Ambientales (IDEAM).
Imbrie, J., Hays, J. D., Martinson, D. G., McIntyre, A., Mix, A. C., Morley, J. J., Pisias, N. G., Prell, W. L., and Shackleton, N. J., The orbital theory of Pleistocene climate: Support from a revised chronology of the marine delta18 O record, *in* Proceedings Milankovitch and climate: Understanding the response to astronomical forcing1984, Volume 1, p. 269.
Kirby, E., and Whipple, K., 2001, Quantifying differential rock-uplift rates via stream profile analysis: Geology, v. 29, no. 5, p. 415-418.
Kirby, E., and Whipple, K. X., 2012, Expression of active tectonics in erosional landscapes: Journal of Structural Geology.
Lal, D., 1991, Cosmic ray labeling of erosion surfaces:< i> in situ</i> nuclide production rates and erosion models: Earth and Planetary Science Letters, v. 104, no. 2, p. 424-439.
Last, N., Plumb, R., Harkness, R., Charlez, P., Alsen, J., and McLean, M., An Integrated Approach to Evaluating and Managing Wellbore Instability in the Cusiana Field Colombia South America, *in*

Proceedings SPE Annual Technical Conference and Exhibition1995, Society of Petroleum Engineers.
Lavé, J., and Avouac, J.-P., 2000, Active folding of fluvial terraces across the Siwaliks Hills, Himalayas of central Nepal: Journal of Geophysical Research: Solid Earth (1978–2012), v. 105, no. B3, p. 5735-5770.
Lavé, J., and Avouac, J., 2001, Fluvial incision and tectonic uplift across the Himalayas of central Nepal: Journal of Geophysical Research: Solid Earth (1978–2012), v. 106, no. B11, p. 26561-26591.
Mercader, J., Gosse, J. C., Bennett, T., Hidy, A. J., and Rood, D. H., 2012, Cosmogenic nuclide age constraints on Middle Stone Age lithics from Niassa, Mozambique: Quaternary Science Reviews, v. 47, p. 116-130.
Miller, S. R., Sak, P. B., Kirby, E., and Bierman, P. R., 2013, Neogene rejuvenation of central Appalachian topography: Evidence for differential rock uplift from stream profiles and erosion rates: Earth and Planetary Science Letters, v. 369, p. 1-12.
Molnar, P., Brown, E. T., Burchfiel, B. C., Deng, Q., Feng, X., Li, J., Raisbeck, G. M., Shi, J., Zhangming, W., and Yiou, F., 1994, Quaternary climate change and the formation of river terraces across growing anticlines on the north flank of the Tien Shan, China: The Journal of Geology, p. 583-602.
Molnar, P., and Cane, M. A., 2002, El Niño's tropical climate and teleconnections as a blueprint for pre-Ice Age climates: Paleoceanography, v. 17, no. 2, p. 11-11-11-11.
Molnar, P., and England, P., 1990, Late Cenozoic uplift of mountain ranges and global climate change: chicken or egg?: Nature, v. 346, no. 6279, p. 29-34.
Montgomery, D. R., Balco, G., and Willett, S. D., 2001, Climate, tectonics, and the morphology of the Andes: Geology, v. 29, no. 7, p. 579-582.
Mora, A., Parra, M., Strecker, M. R., Kammer, A., Dimaté, C., and Rodríguez, F., 2006, Cenozoic contractional reactivation of Mesozoic extensional structures in the Eastern Cordillera of Colombia: Tectonics, v. 25, no. 2, p. TC2010.
Mora, A., Parra, M., Strecker, M. R., Sobel, E. R., Hooghiemstra, H., Torres, V., and Jaramillo, J. V., 2008, Climatic forcing of asymmetric orogenic evolution in the Eastern Cordillera of Colombia: Geological Society of America Bulletin, v. 120, no. 7-8, p. 930-949.
Mora, A., Parra, M., Strecker, M. R., Sobel, E. R., Zeilinger, G., Jaramillo, C., Da Silva, S. F., and Blanco, M., 2010, The eastern foothills of the Eastern Cordillera of Colombia: An example of multiple factors controlling structural styles and active tectonics: Geological Society of America Bulletin, v. 122, no. 11-12, p. 1846-1864.
Mora, A., Reyes-Harker, A., Rodriguez, G., Tesón, E., Ramirez-Arias, J. C., Parra, M., Caballero, V., Mora, J. P., Quintero, I., and Valencia, V., 2013, Inversion tectonics under increasing rates of shortening and sedimentation: Cenozoic example from the Eastern Cordillera of Colombia: Geological Society, London, Special Publications, v. 377, no. 1, p. 411-442.
Ouimet, W. B., Whipple, K. X., and Granger, D. E., 2009, Beyond threshold hillslopes: Channel adjustment to base-level fall in tectonically active mountain ranges: Geology, v. 37, no. 7, p. 579-582.
Parra, M., Mora, A., Jaramillo, C., Torres, V., Zeilinger, G., and Strecker, M. R., 2010, Tectonic controls on Cenozoic foreland basin development in the north-eastern Andes, Colombia: Basin Research, v. 22, no. 6, p. 874-903.
Parra, M., Mora, A., Sobel, E. R., Strecker, M. R., and González, R., 2009, Episodic orogenic front migration in the northern Andes: Constraints from low-temperature thermochronology in the Eastern Cordillera, Colombia: Tectonics, v. 28, no. 4, p. TC4004.
Pérez, O. J., Bilham, R., Sequera, M., Molina, L., Gavotti, P., Moncayo, C., Rodríguez, C., Guzmán, M., Codallo, H., and Velandia, R., 2011, Campo de velocidades GPS en el occidente de Venezuela:

Componente lateral derecha asociada a la Falla de Boconó y componente convergente perpendicular a Los Andes: Interciencia, no. 1, p. 39-44.
Rowan, M. G., and Linares, R., 2000, Fold-evolution matrices and axial-surface analysis of fault-bend folds: application to the Medina anticline, eastern Cordillera, Colombia: AAPG bulletin, v. 84, no. 6, p. 741-764.
RSNC, 2015, Consultas de Sismicidad, *in* (RSNC), R. S. N. d. C., ed.: http://seisan.sgc.gov.co/RSNC/index.php/consultas.
Safran, E. B., Bierman, P. R., Aalto, R., Dunne, T., Whipple, K. X., and Caffee, M., 2005, Erosion rates driven by channel network incision in the Bolivian Andes: Earth Surface Processes and Landforms, v. 30, no. 8, p. 1007-1024.
Silva, A., 2010, Cinemática de la deformación frágil en el área de medina (Cordillera Oriental, Colombia); Relación de temporalidad entre la deformación frágil y los sistemas petrolíferos. [Master's: Universidad Industrial de Santander, 122 p.
Simoes, M., Avouac, J. P., and Chen, Y. G., 2007, Slip rates on the Chelungpu and Chushiang thrust faults inferred from a deformed strath terrace along the Dungpuna river, west central Taiwan: Journal of Geophysical Research: Solid Earth (1978–2012), v. 112, no. B3.
Snyder, N. P., Whipple, K. X., Tucker, G. E., and Merritts, D. J., 2000, Landscape response to tectonic forcing: Digital elevation model analysis of stream profiles in the Mendocino triple junction region, northern California: Geological Society of America Bulletin, v. 112, no. 8, p. 1250-1263.
Stone, J. O., 2000, Air pressure and cosmogenic isotope production: Journal of Geophysical Research: Solid Earth (1978–2012), v. 105, no. B10, p. 23753-23759.
Strecker, M., Alonso, R., Bookhagen, B., Carrapa, B., Hilley, G., Sobel, E., and Trauth, M., 2007, Tectonics and climate of the southern central Andes: Annu. Rev. Earth Planet. Sci., v. 35, p. 747-787.
Taboada, A., Rivera, L. A., Fuenzalida, A., Cisternas, A., Philip, H., Bijwaard, H., Olaya, J., and Rivera, C., 2000, Geodynamics of the northern Andes: Subductions and intracontinental deformation (Colombia): Tectonics, v. 19, no. 5, p. 787-813.
Tapponnier, P., Ryerson, F. J., Van der Woerd, J., Mériaux, A.-S., and Lasserre, C., 2001, Long-term slip rates and characteristic slip: keys to active fault behaviour and earthquake hazard: Comptes Rendus de l'Académie des Sciences-Series IIA-Earth and Planetary Science, v. 333, no. 9, p. 483-494.
Taylor, M. H., Kapp, P. A., and Horton, B. K., 2012, Basin Response to Active Extension and Strike-Slip Deformation in the Hinterland of the Tibetan Plateau: Tectonics of Sedimentary Basins, p. 445-460.
Tesón, E., Mora, A., Silva, A., Namson, J., Teixell, A., Castellanos, J., Casallas, W., Julivert, M., Taylor, M., and Ibáñez-Mejía, M., 2013, Relationship of Mesozoic graben development, stress, shortening magnitude, and structural style in the Eastern Cordillera of the Colombian Andes: Geological Society, London, Special Publications, v. 377, no. 1, p. 257-283.
Toro, J., Roure, F., Bordas-Le Floch, N., Le Cornec-Lance, S., and Sassi, W., 2004, Thermal and kinematic evolution of the Eastern Cordillera fold and thrust belt, Colombia.
Trenkamp, R., Kellogg, J. N., Freymueller, J. T., and Mora, H. P., 2002, Wide plate margin deformation, southern Central America and northwestern South America, CASA GPS observations: Journal of South American Earth Sciences, v. 15, no. 2, p. 157-171.
USGS, 2014, Earthquake Hazards Program, Volume 2014.
van der Hammen, T., and Hooghiemstra, H., 2000, Neogene and Quaternary history of vegetation, climate, and plant diversity in Amazonia: Quaternary Science Reviews, v. 19, no. 8, p. 725-742.
Veloza, G., Styron, R., Taylor, M., and Mora, A., 2012, Open-source archive of active faults for northwest South America: GSA Today, v. 22, no. 10.

Veloza, G., Taylor, M., Mora, A., and Gosse, J., 2015, Active mountain building along the eastern Colombian Sub-Andes: A folding history from fluvial terraces across the Tame anticline, Llanos basin: Geological Society of America Bulletin, v. Accepted.

Villamil, T., 2003, Regional hydrocarbon systems of Colombia and western Venezuela: Their origin, potential, and exploration, *in* Bartolini, C., Buffler, R. T., and Blickwede, J., eds., The Circum-Gulf of Mexico and the Caribbean: Hydrocarborn habitats, basin formation, and plate tectonics, Volume 79: AAPG Memoir, p. 697-734.

Whipple, K., Wobus, C., Crosby, B., Kirby, E., and Sheehan, D., New tools for quantitative geomorphology: extraction and interpretation of stream profiles from digital topographic data, *in* Proceedings Geological Society of America, Annual Meeting, Short Course Guide, Boulder, Colorado, 2007, Volume 506: (available on the web at: http://www.geomorphtools.org).

Wobus, C., Whipple, K. X., Kirby, E., Snyder, N., Johnson, J., Spyropolou, K., Crosby, B., and Sheehan, D., 2006, Tectonics from topography: Procedures, promise, and pitfalls: SPECIAL PAPERS-GEOLOGICAL SOCIETY OF AMERICA, v. 398, p. 55.

Youngs, R. R., and Coppersmith, K. J., 1985, Implications of fault slip rates and earthquake recurrence models to probabilistic seismic hazard estimates: Bulletin of the Seismological society of America, v. 75, no. 4, p. 939-964.

Supplementary Figures

Supplementary Figure 1

Site M1

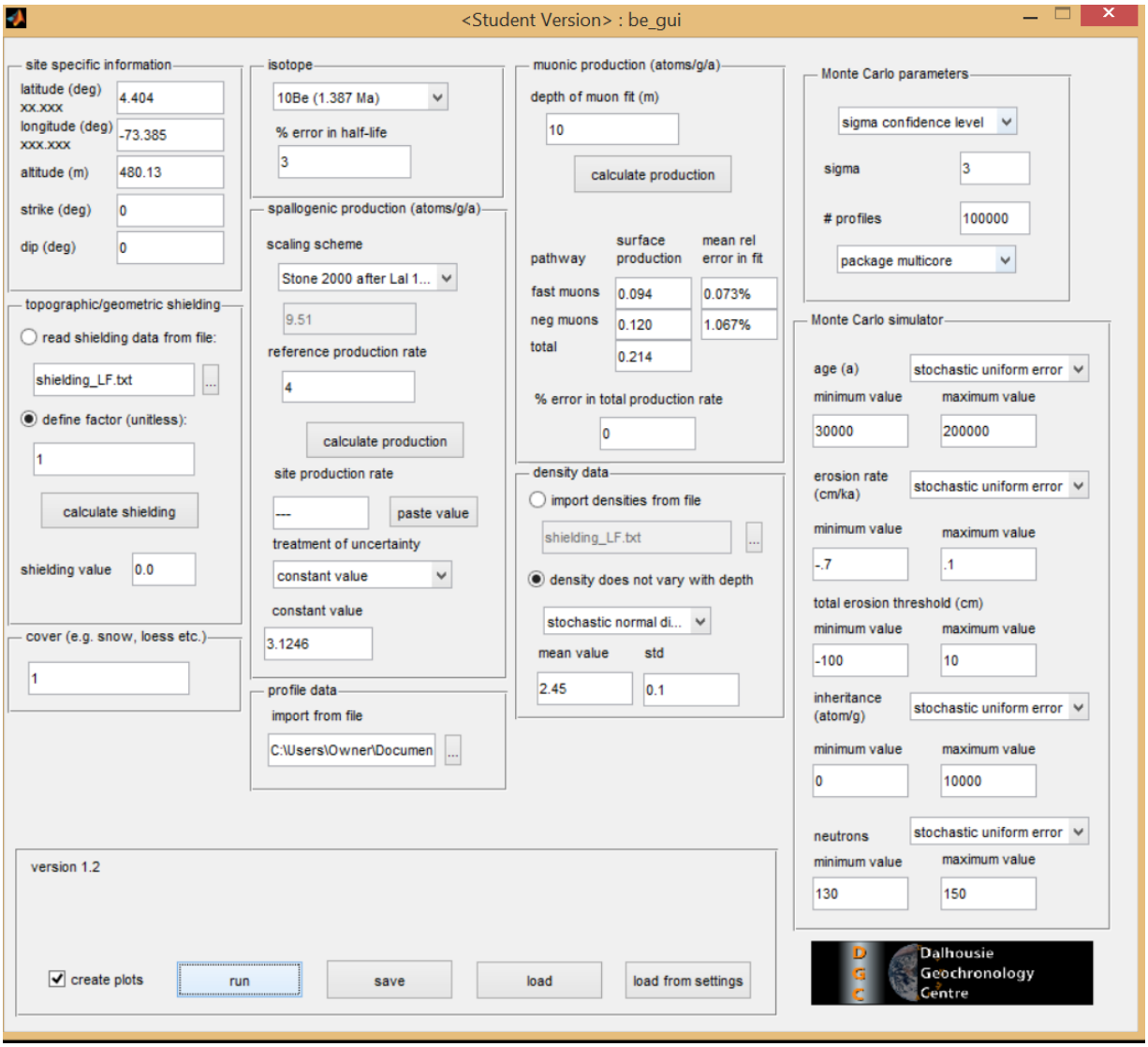

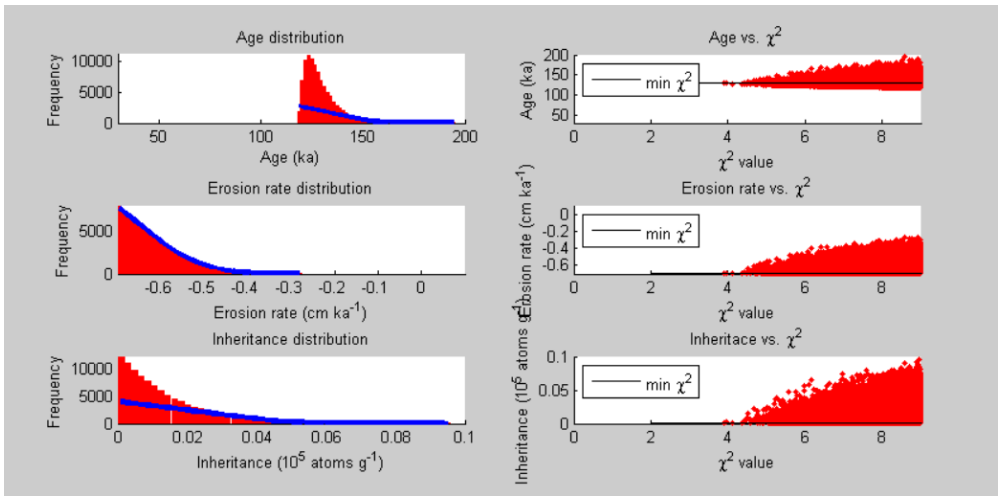
Age distribution
Frequency
Age (ka)
Age vs. χ^2
Age (ka)
min χ^2
χ^2 value
Erosion rate distribution
Frequency
Erosion rate (cm ka^{-1})
Erosion rate vs. χ^2
Erosion rate (cm ka^{-1})
min χ^2
χ^2 value
Inheritance distribution
Frequency
Inheritance (10^5 atoms g^{-1})
Inheritace vs. χ^2
Inheritance (10^5 atoms g^{-1})
min χ^2
χ^2 value

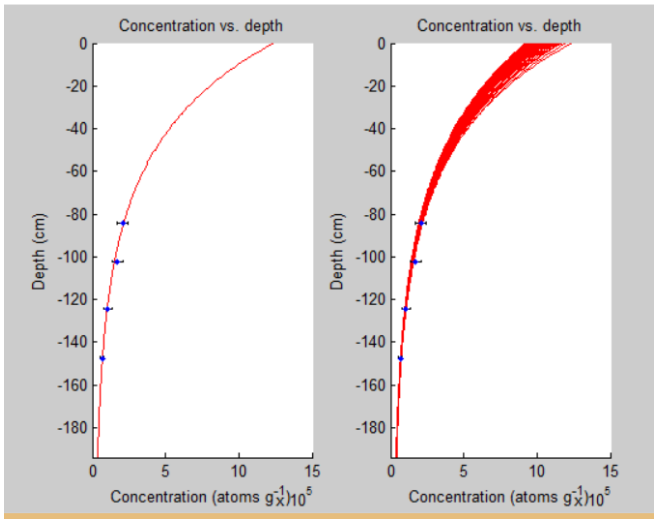
Concentration vs. depth
Depth (cm)
Concentration (atoms g^{-1})10^5
Concentration vs. depth
Depth (cm)
Concentration (atoms g^{-1})10^5

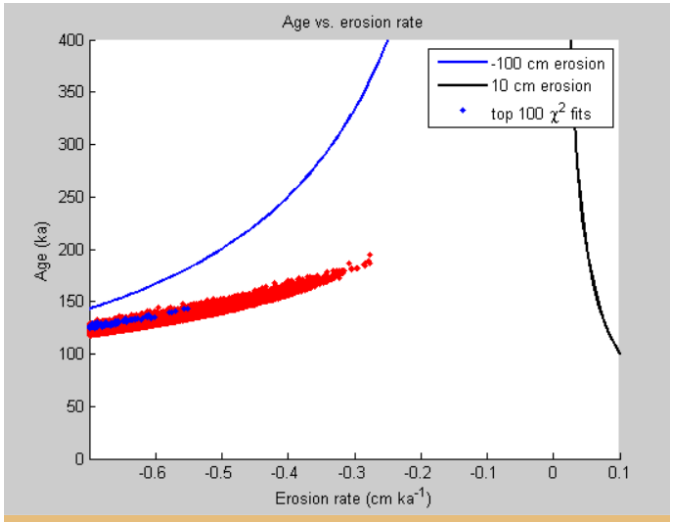
Age vs. erosion rate
-100 cm erosion
10 cm erosion
top 100 χ^2 fits
Age (ka)
Erosion rate (cm ka^{-1})

Site M2

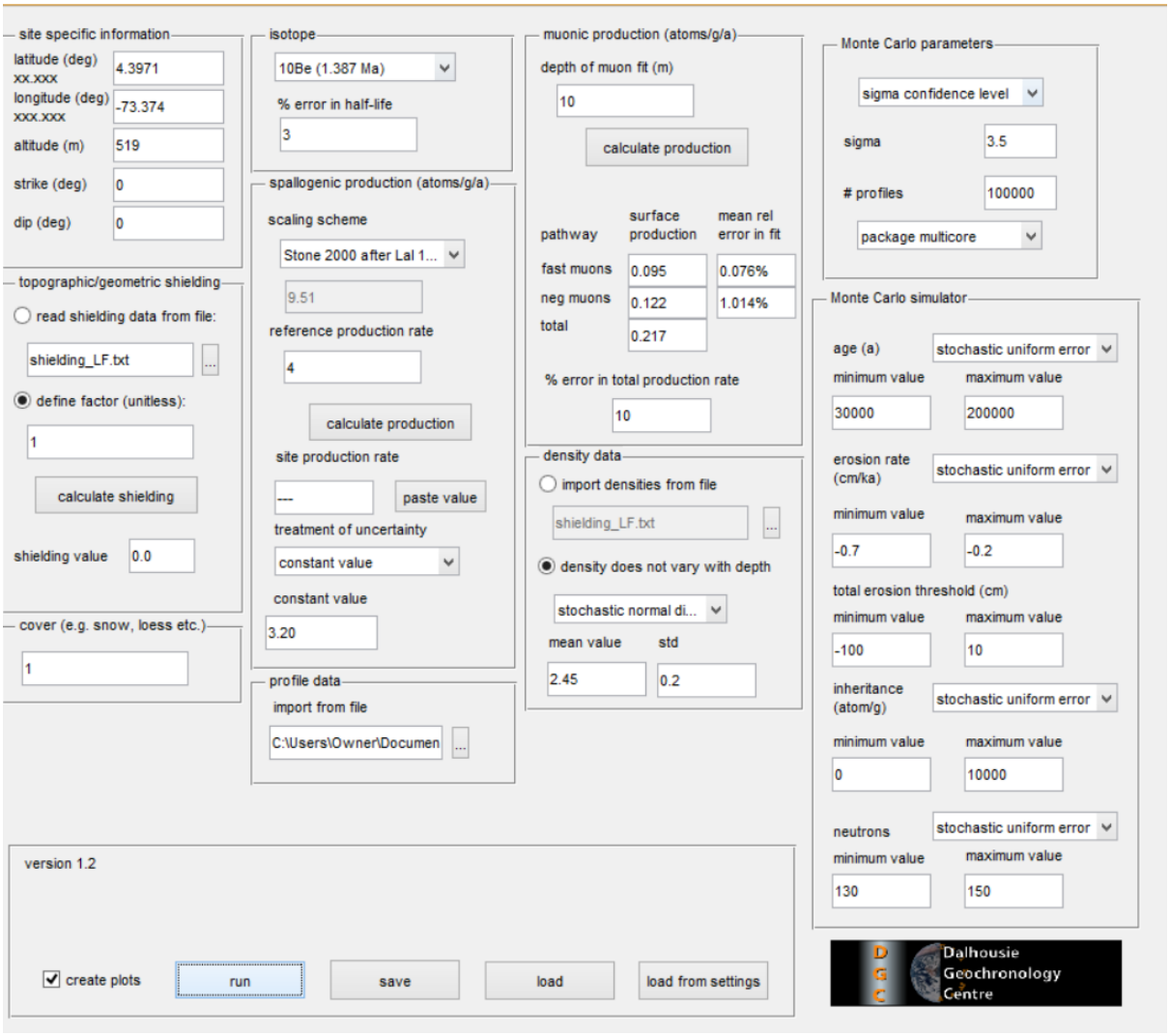
site specific information
latitude (deg) xx.xxx
4.3971
longitude (deg) xxx.xxx
-73.374
altitude (m)
519
strike (deg)
0
dip (deg)
0
topographic/geometric shielding
read shielding data from file:
shielding_LF.txt
define factor (unitless):
1
calculate shielding
shielding value
0.0
cover (e.g. snow, loess etc.)
1
isotope
10Be (1.387 Ma)
% error in half-life
3
spallogenic production (atoms/g/a)
scaling scheme
Stone 2000 after Lal 1...
9.51
reference production rate
4
calculate production
site production rate
---
paste value
treatment of uncertainty
constant value
constant value
3.20
profile data
import from file
C:\Users\Owner\Documen
muonic production (atoms/g/a)
depth of muon fit (m)
10
calculate production
pathway
surface production
mean rel error in fit
fast muons
0.095
0.076%
neg muons
0.122
1.014%
total
0.217
% error in total production rate
10
density data
import densities from file
shielding_LF.txt
density does not vary with depth
stochastic normal di...
mean value
std
2.45
0.2
Monte Carlo parameters
sigma confidence level
sigma
3.5
profiles
100000
package multicore
Monte Carlo simulator
age (a)
stochastic uniform error
minimum value
maximum value
30000
200000
erosion rate (cm/ka)
stochastic uniform error
minimum value
maximum value
-0.7
-0.2
total erosion threshold (cm)
minimum value
maximum value
-100
10
inheritance (atom/g)
stochastic uniform error
minimum value
maximum value
0
10000
neutrons
stochastic uniform error
minimum value
maximum value
130
150
version 1.2
create plots
run
save
load
load from settings
Dalhousie Geochronology Centre

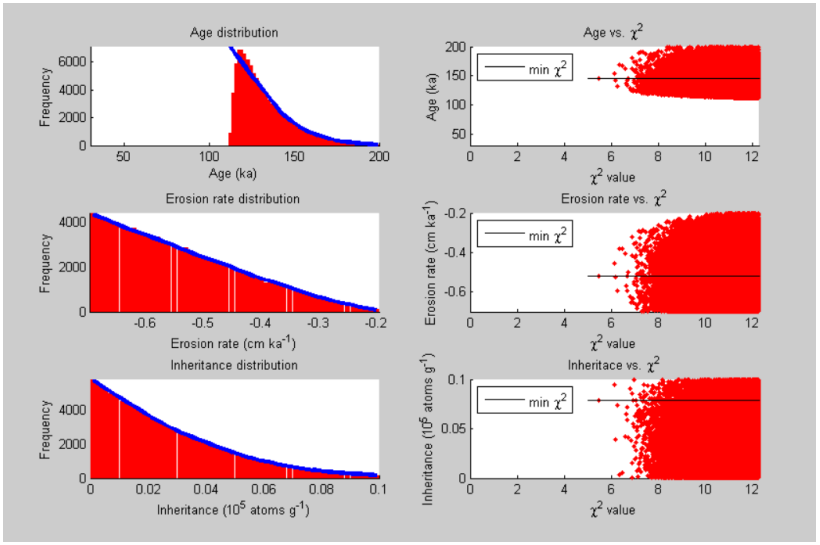
Age distribution
Frequency
Age (ka)
Age vs. χ2
min χ2
Age (ka)
χ2 value
Erosion rate distribution
Frequency
Erosion rate (cm ka-1)
Erosion rate vs. χ2
min χ2
Erosion rate (cm ka-1)
χ2 value
Inheritance distribution
Frequency
Inheritance (10^5 atoms g-1)
Inheritace vs. χ2
min χ2
Inheritance (10^5 atoms g-1)
χ2 value

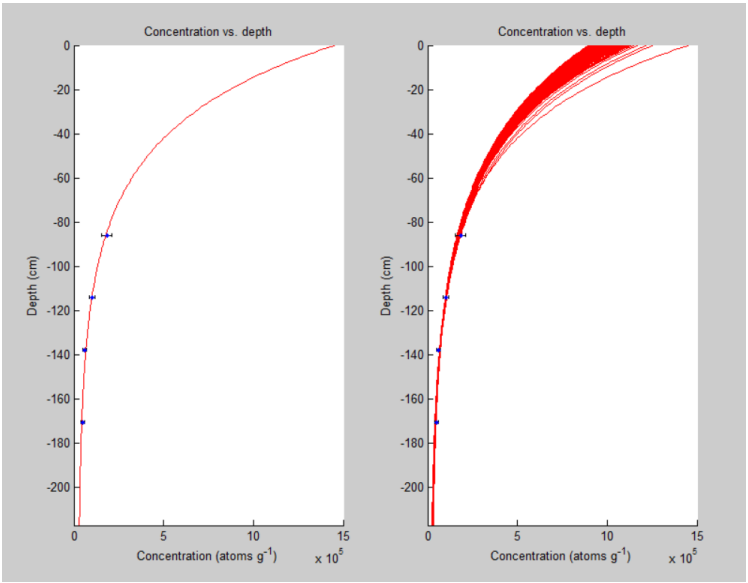
Concentration vs. depth
Depth (cm)
Concentration (atoms g-1)
x 10^5
Concentration vs. depth
Depth (cm)
Concentration (atoms g-1)
x 10^5

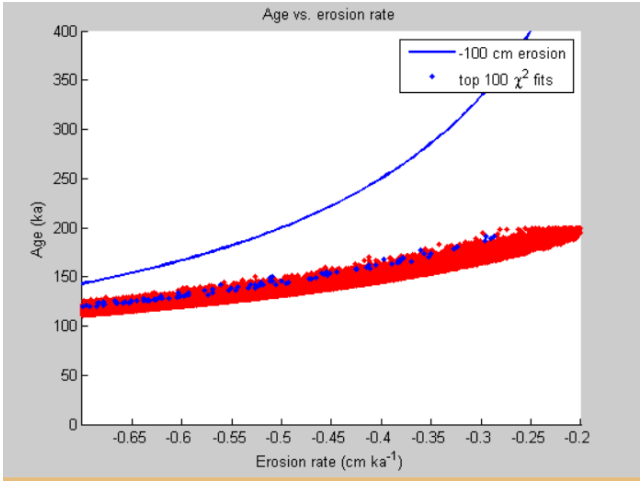
Age vs. erosion rate
-100 cm erosion
top 100 χ2 fits
Age (ka)
Erosion rate (cm ka-1)

Supplementary Figure 1. Results from depth profile Monte Carlo modeling using codes from Hidy et al. (2010) for site M1 and M2. Input parameters and resulting plots are shown for each site. Profile fit solutions were not found below a 3.5σ error on the concentrations.

Supplementary Figure 2

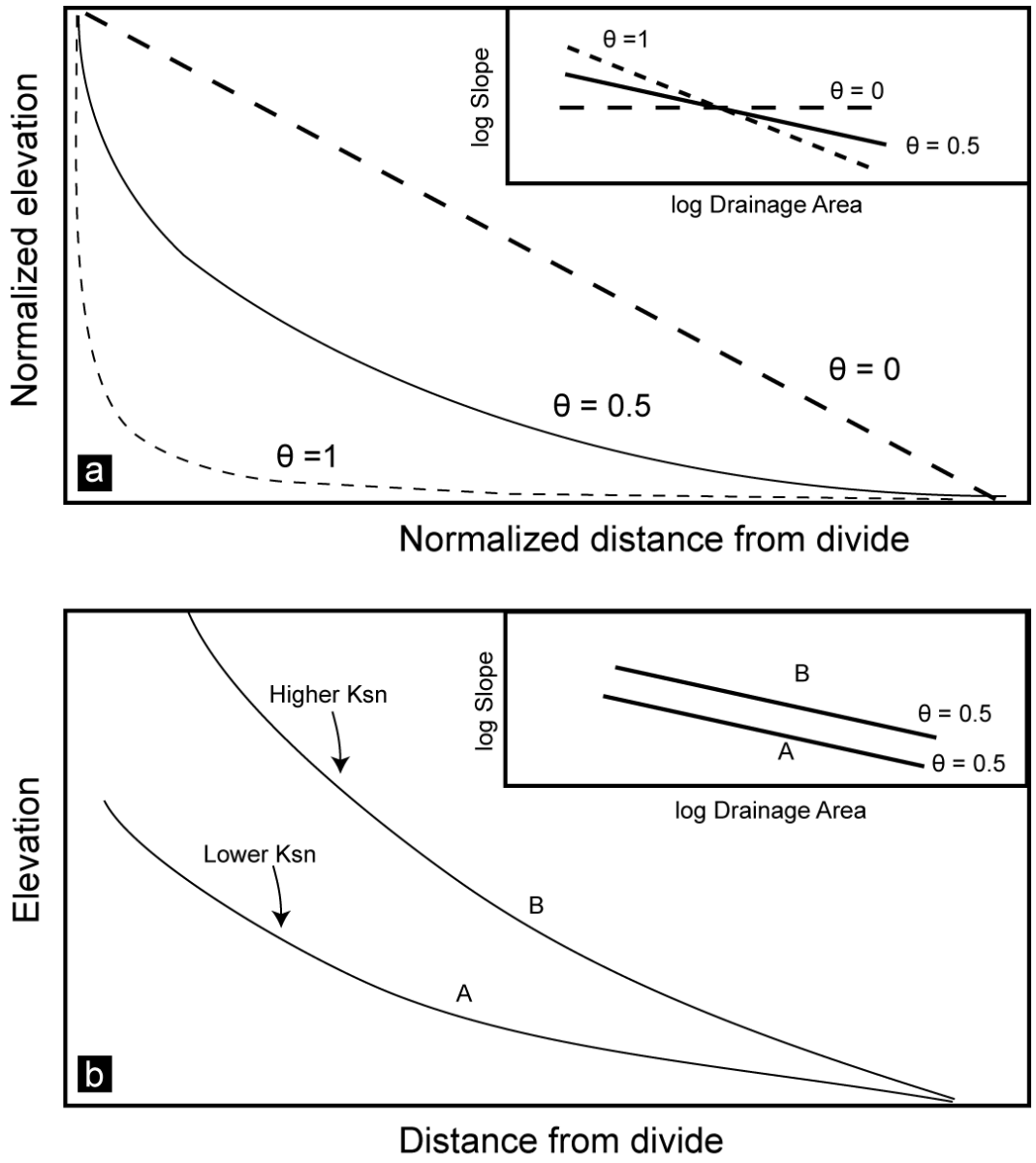

Supplementary Figure 2. Schematic stream profile plots modified from Kirby and Whipple (2012). A) Longitudinal stream profile of 3 streams with varying concavities. The inset log plot shows where the data values are extracted from. B) Longitudinal stream profiles exhibiting 2 different k_{sn} values and the same concavity. Inset log plot highlights that these streams have the same slope, but different y-intercepts.

Supplementary Figure 3

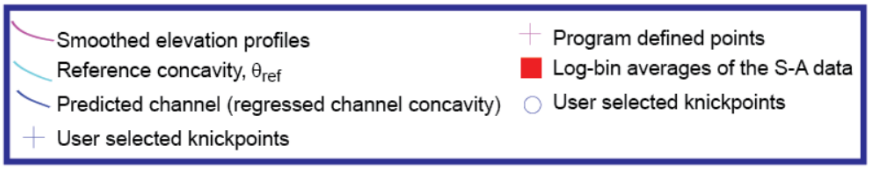

AA

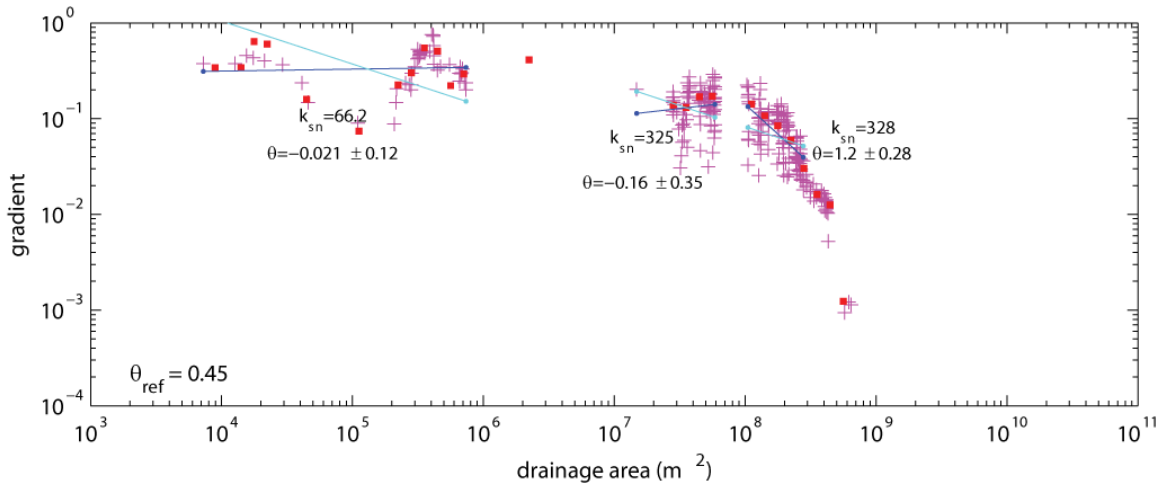

BB

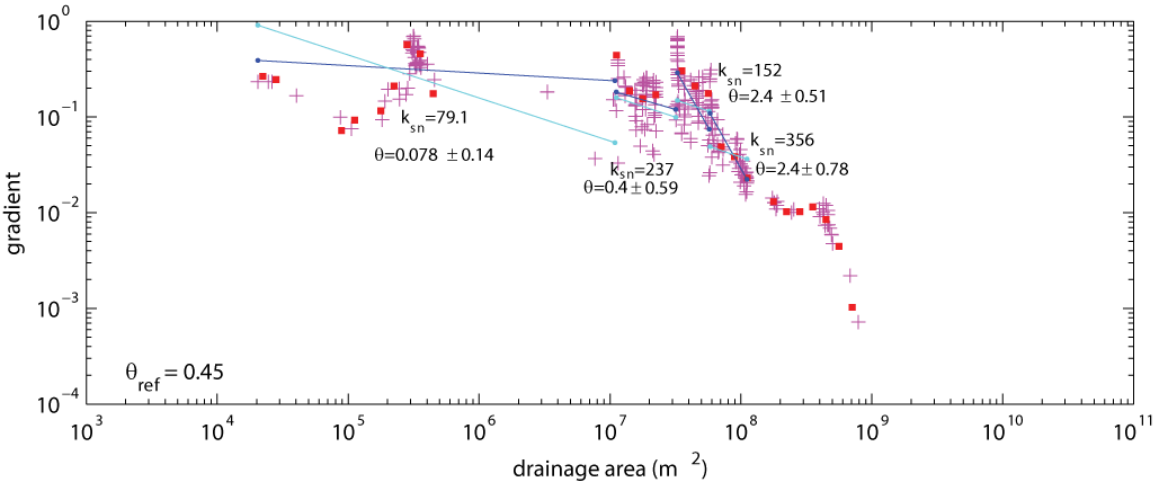

CC

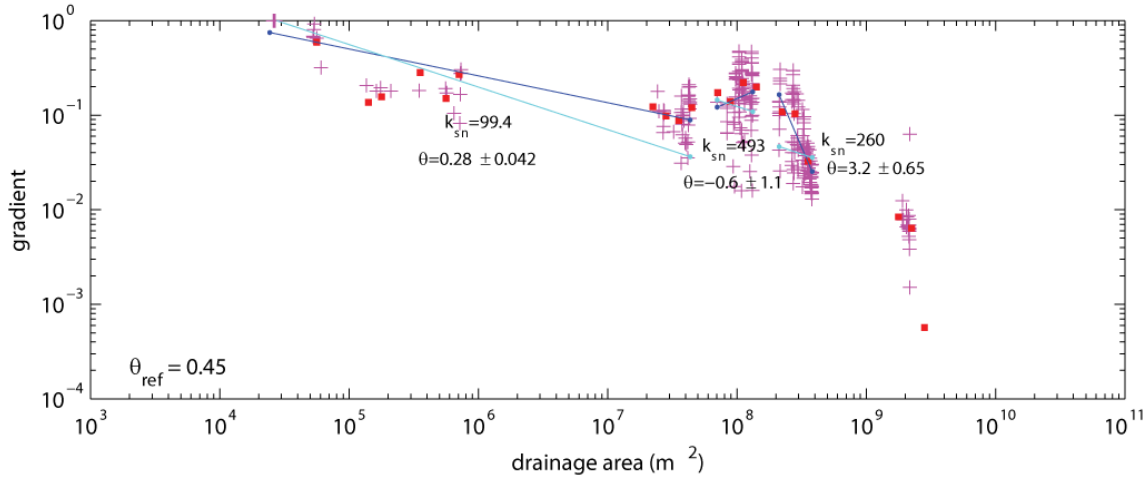
gradient
drainage area (m 2)
θref = 0.45
ksn=99.4
θ=0.28 ±0.042
ksn=493
θ=−0.6 ±1.1
ksn=260
θ=3.2 ±0.65

DD

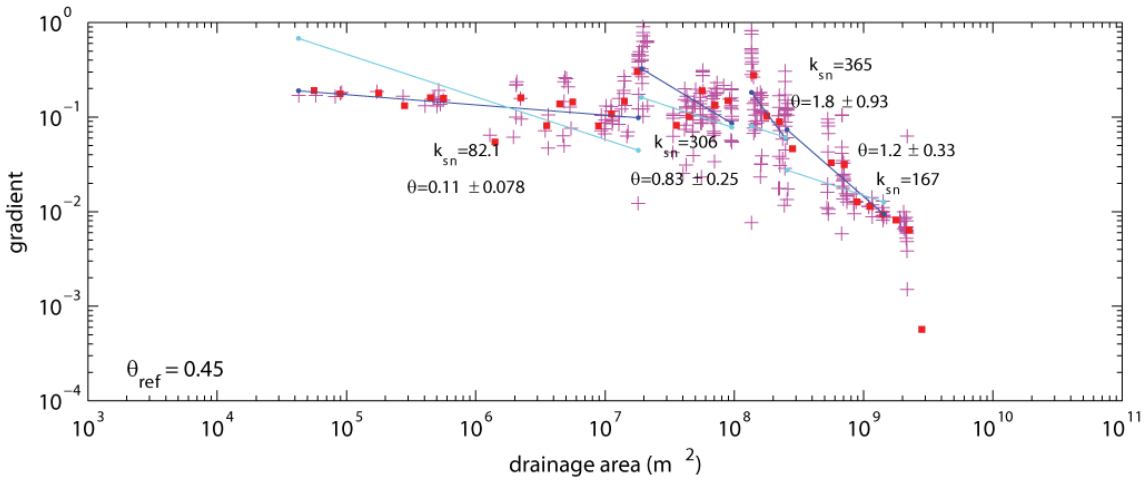
gradient
drainage area (m 2)
θref = 0.45
ksn=82.1
θ=0.11 ±0.078
ksn=306
θ=0.83 ±0.25
ksn=365
θ=1.8 ±0.93
θ=1.2 ±0.33
ksn=167

EE

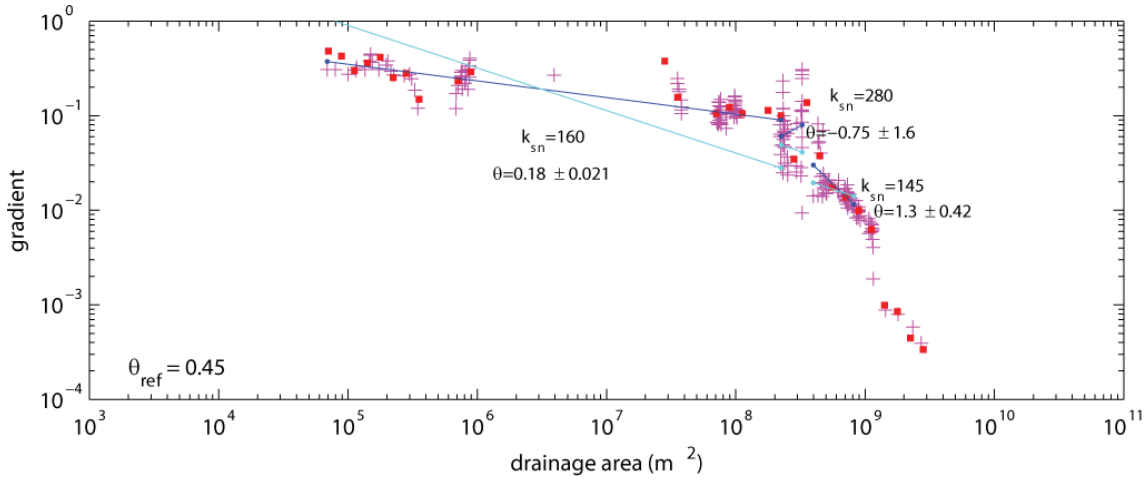
gradient
drainage area (m 2)
θref = 0.45
ksn=160
θ=0.18 ±0.021
ksn=280
θ=−0.75 ±1.6
ksn=145
θ=1.3 ±0.42

FF

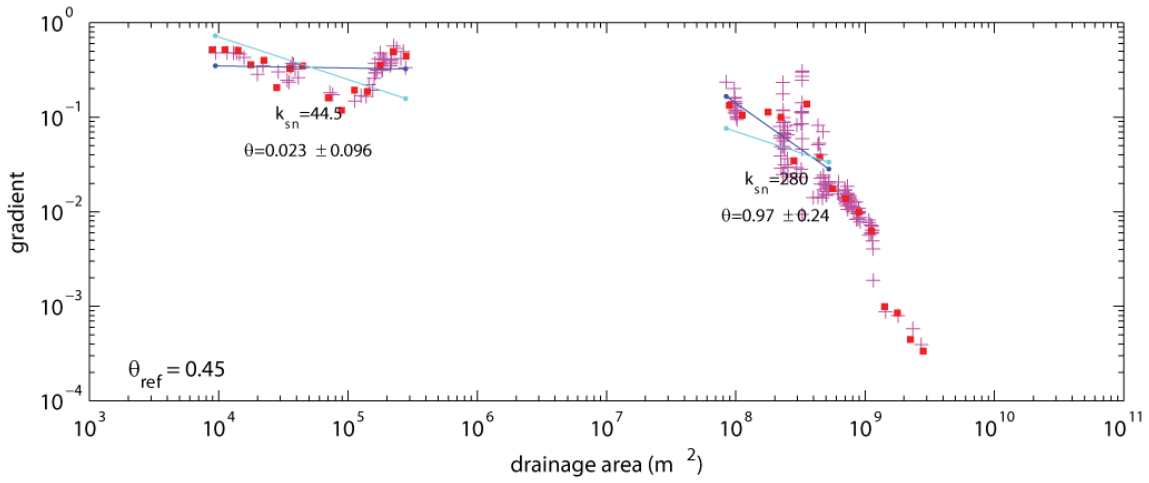
gradient
drainage area (m 2)
θref = 0.45
ksn=44.5
θ=0.023 ±0.096
ksn=280
θ=0.97 ±0.24

GG

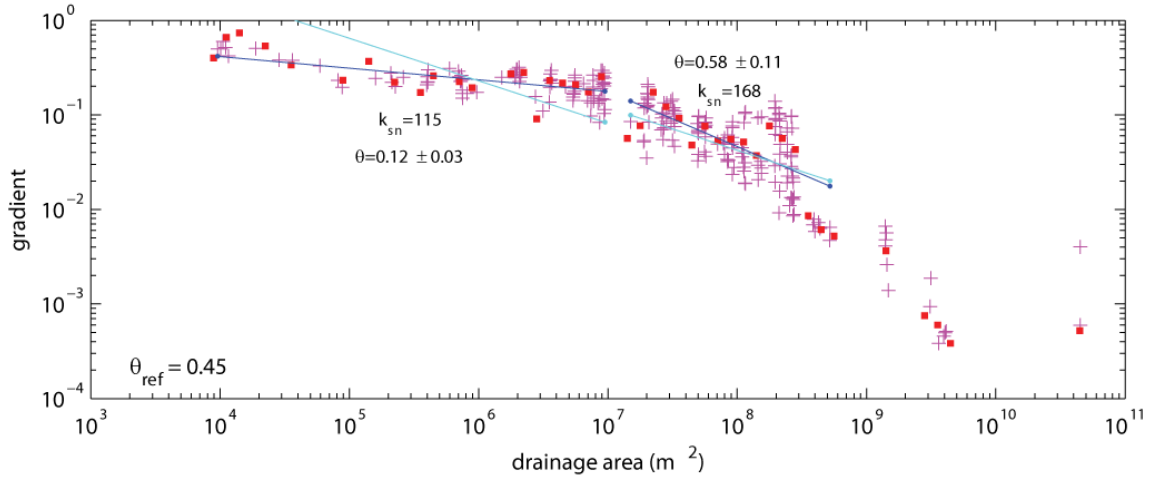
gradient
drainage area (m 2)
θref = 0.45
ksn=115
θ=0.12 ±0.03
θ=0.58 ±0.11
ksn=168

II

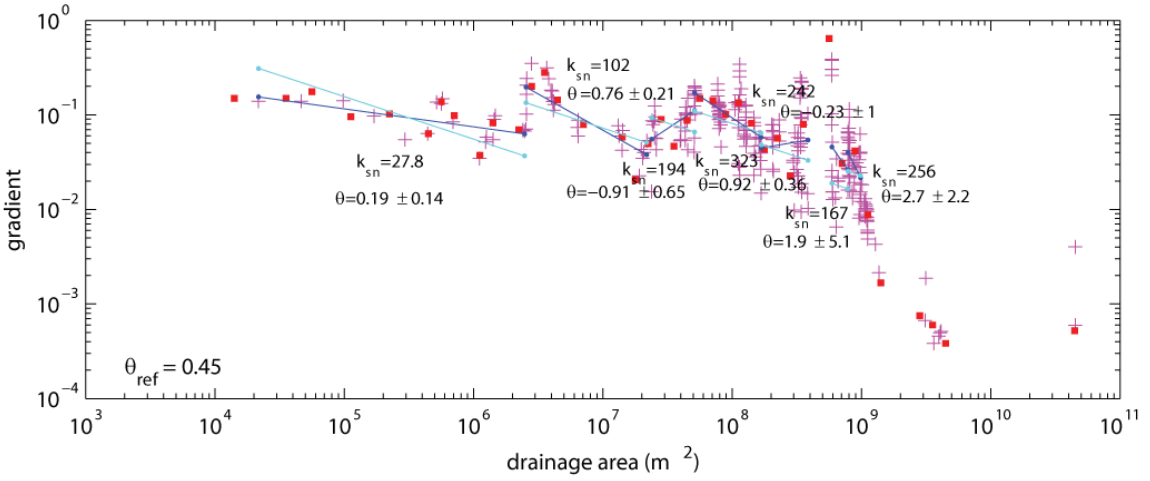
gradient
drainage area (m 2)
θref = 0.45
ksn=27.8
θ=0.19 ±0.14
ksn=102
θ=0.76 ±0.21
ksn=194
θ=−0.91 ±0.65
ksn=242
θ=0.23 ±1
ksn=323
θ=0.92 ±0.36
ksn=167
θ=1.9 ±5.1
ksn=256
θ=2.7 ±2.2

JJ

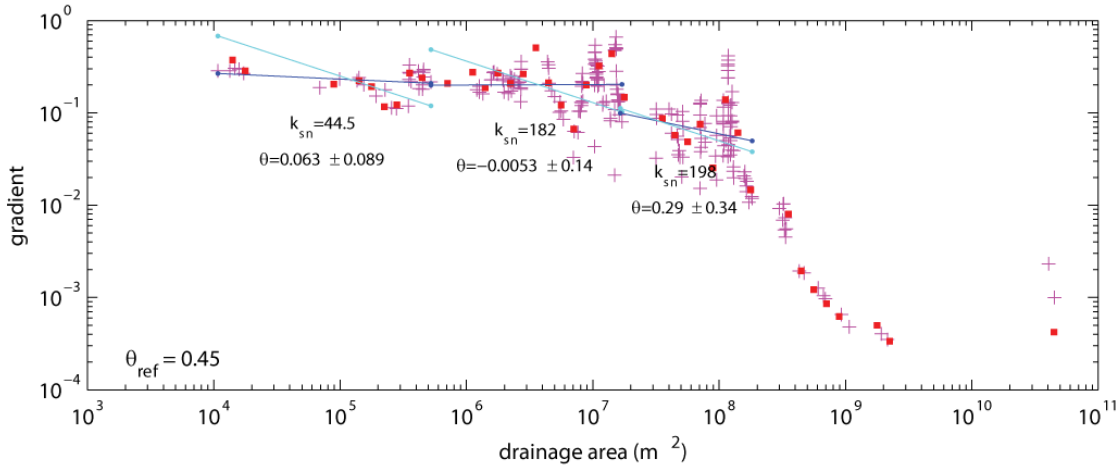
gradient
drainage area (m 2)
θref = 0.45
ksn=44.5
θ=0.063 ±0.089
ksn=182
θ=−0.0053 ±0.14
ksn=198
θ=0.29 ±0.34

LL

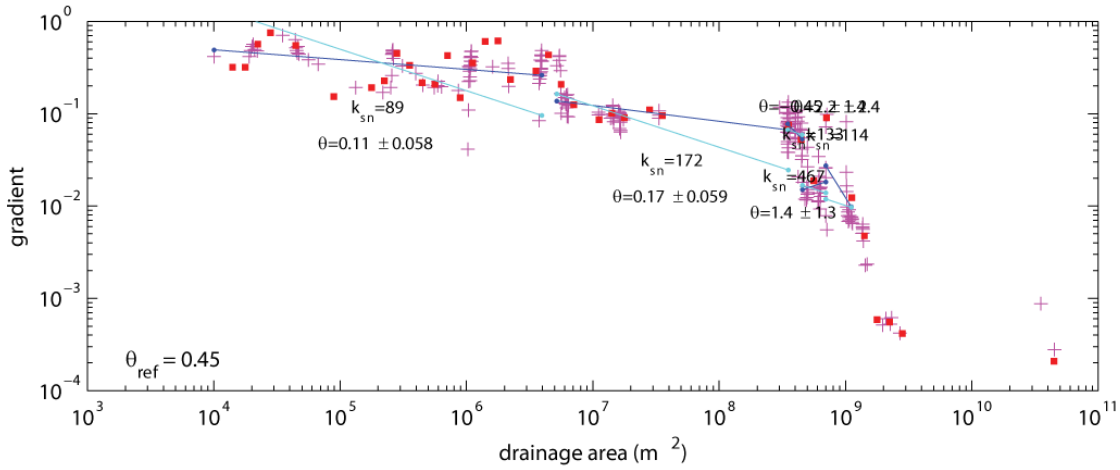
gradient
drainage area (m 2)
θref = 0.45
ksn=89
θ=0.11 ±0.058
ksn=172
θ=0.17 ±0.059
ksn=467
θ=1.4 ±1.3

MM

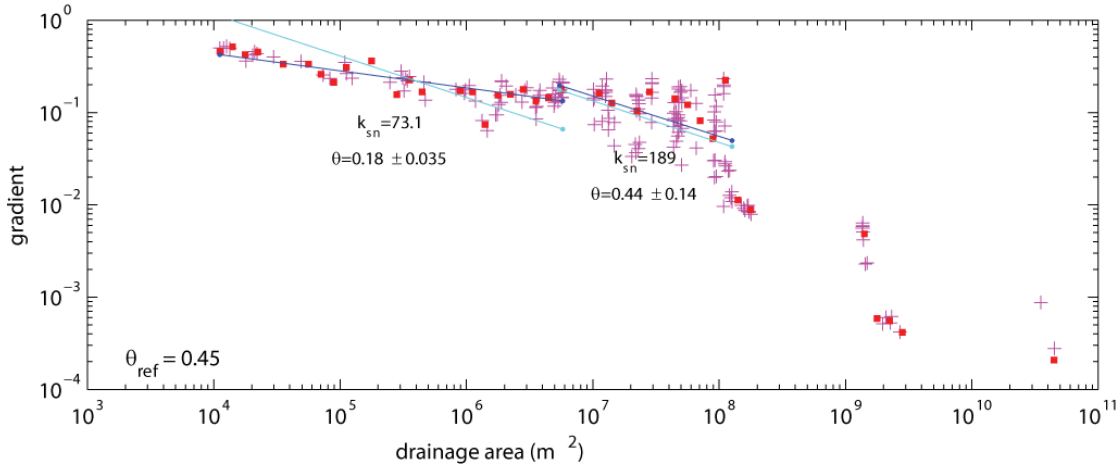
gradient
drainage area (m 2)
θref = 0.45
ksn=73.1
θ=0.18 ±0.035
ksn=189
θ=0.44 ±0.14

NN

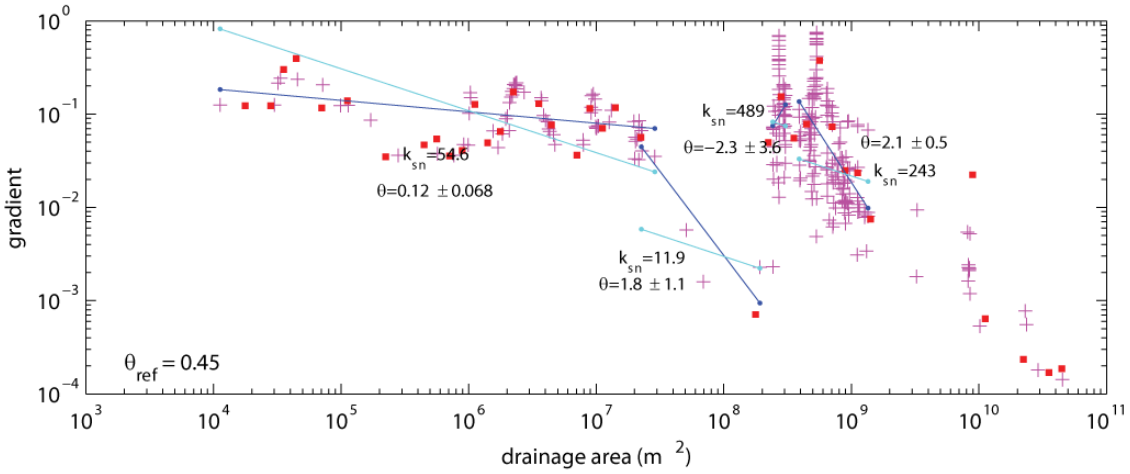
gradient
drainage area (m 2)
θref = 0.45
ksn=54.6
θ=0.12 ±0.068
ksn=11.9
θ=1.8 ±1.1
ksn=489
θ=−2.3 ±3.6
θ=2.1 ±0.5
ksn=243

OO

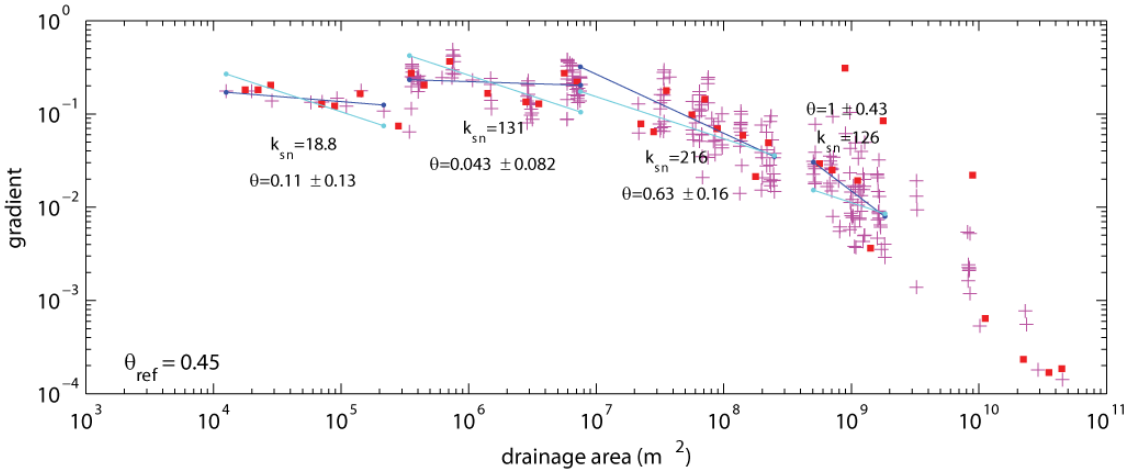
gradient
drainage area (m 2)
θref = 0.45
ksn=18.8
θ=0.11 ±0.13
ksn=131
θ=0.043 ±0.082
ksn=216
θ=0.63 ±0.16
θ=1 ±0.43
ksn=126

PP

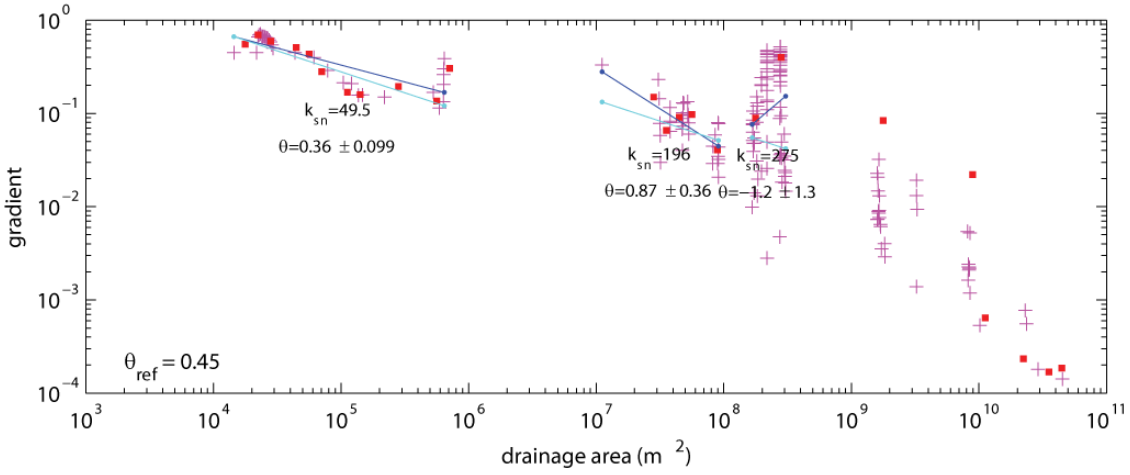
gradient
drainage area (m 2)
θref = 0.45
ksn=49.5
θ=0.36 ±0.099
ksn=196
θ=0.87 ±0.36
ksn=275
θ=−1.2 ±1.3

QQ

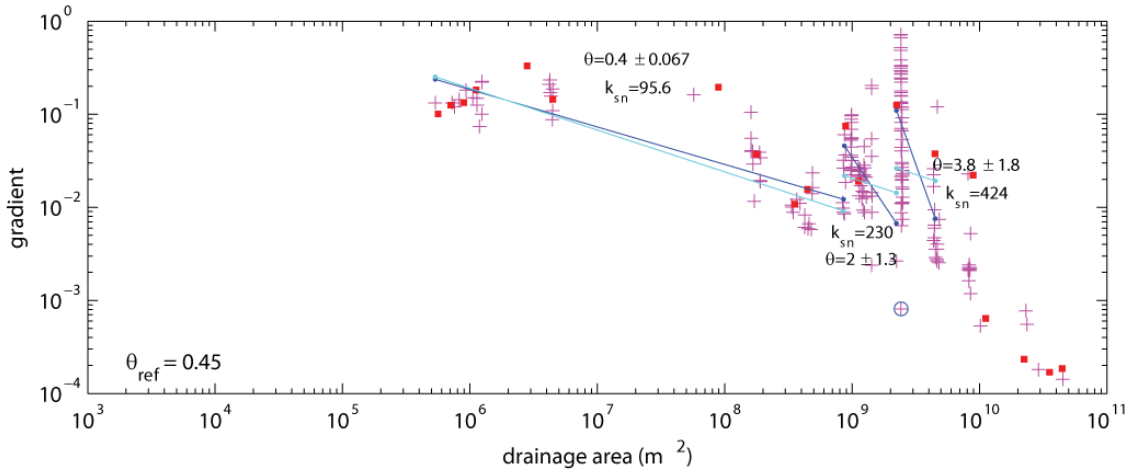
θ=0.4 ±0.067
k_sn=95.6
θ=3.8 ±1.8
k_sn=424
k_sn=230
θ=2 ±1.3
θ_ref = 0.45
gradient
drainage area (m 2)

RR

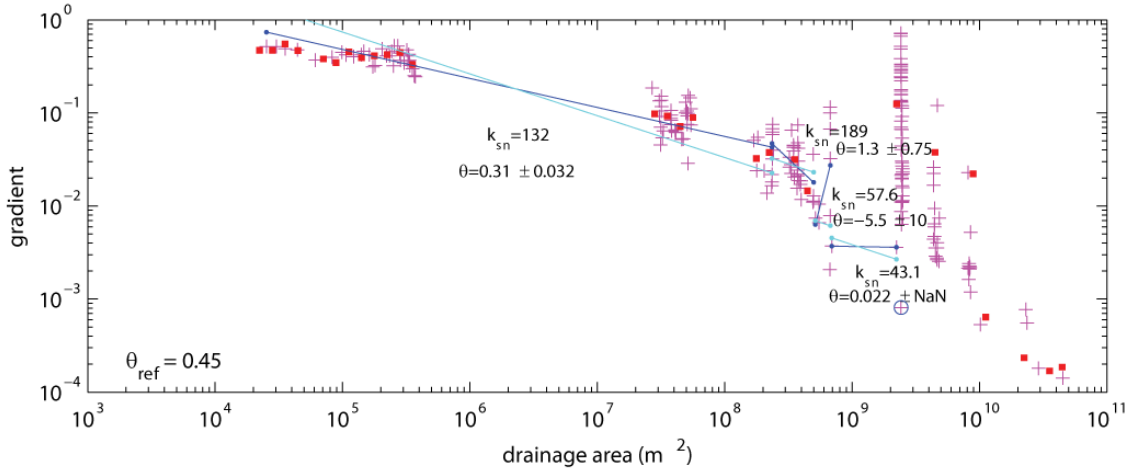
k_sn=132
θ=0.31 ±0.032
k_sn=189
θ=1.3 ±0.75
k_sn=57.6
θ=−5.5 ±10
k_sn=43.1
θ=0.022 ±NaN
θ_ref = 0.45
gradient
drainage area (m 2)

SS

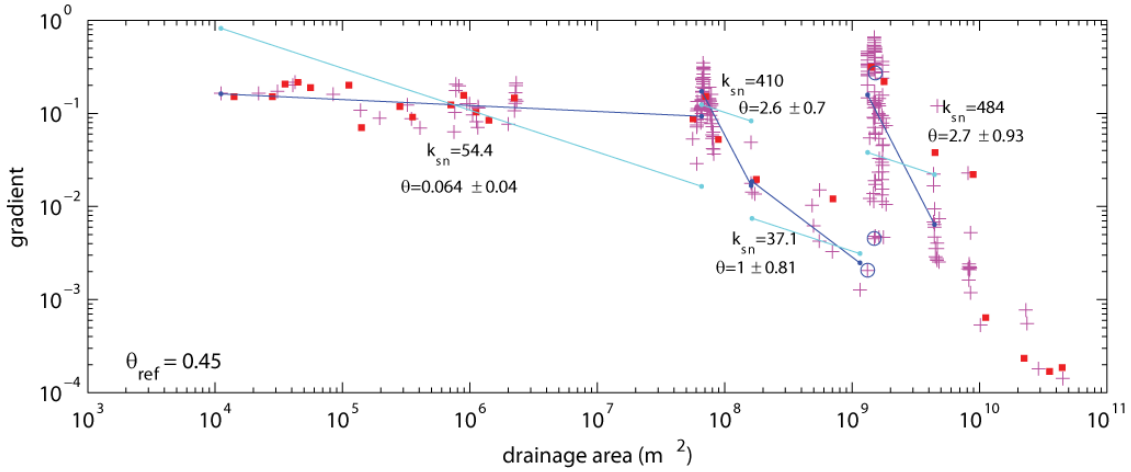
k_sn=410
θ=2.6 ±0.7
k_sn=484
θ=2.7 ±0.93
k_sn=54.4
θ=0.064 ±0.04
k_sn=37.1
θ=1 ±0.81
θ_ref = 0.45
gradient
drainage area (m 2)

Supplementary Figure 3. Log plots of gradient vs. drainage area for all primary streams shown in Figures 9 and 10. Plots are shown from north (AA) to south (SS).